Microphysical modelling of aerosol scavenging by different types of clouds.

Description and validation of the approach

Pascal Lemaitre[1], Arnaud Quérel[2], Alexis Dépée[1], Alice Guerra Devigne[1], Marie Monier[3,4], Thibault Hiron[3], Chloé Soto Minguez[1], Daniel Hardy[5], Andrea Flossmann[3,4]

[1] { Institut de Radioprotection et de Sûreté Nucléaire (IRSN), PSN-RES/SCA/LPMA, F-91400, Saclay, France}

[2] { Institut de Radioprotection et de Sûreté Nucléaire (IRSN), PSE-SANTE/SESUC/BMCA, F-92260, Fontenay-aux-Roses, France}

[3] {Clermont University, Blaise Pascal University, Physical Meteorology Laboratory, Clermont-Ferrand, France}

[4] {CNRS, INSU, UMR 6016, LaMP, Aubière, France}

[5] {School of Chemistry, University of Bristol, Bristol, BS8 1TS, United Kingdom.

Correspondence to: P. Lemaitre (pascal.lemaitre@irsn.fr & arnaud.querel@irsn.fr)

Short abstract

A new in-cloud scavenging scheme is proposed. It is based on a microphysical model of cloud formation and may be applied to long-distance atmospheric transport models (>100 km) and climatic models. This model is applied to for the two most extreme precipitating cloud types, in terms of both relative humidity and vertical extension: cumulonimbus and stratus.

Abstract

With dry deposition and below-cloud scavenging, in-cloud scavenging is one of the three components of aerosol transfer from the atmosphere to the ground. There is no experimental validation of in-cloud particle scavenging models for all cloud types that is not impacted by uncertainties concerning below-cloud scavenging. In this article, the choice was made to start with a recognised and validated microphysical cloud formation model (DESCAM) to extract a scheme of aerosol scavenging by clouds, valid for different cloud types. The resulting model works for the two most extreme precipitation clouds: from cumulonimbus to stratus. It is based on data accessible a priori from Numerical Weather Prediction (NWP) outputs, i.e., the intensity of the rain and the relative humidity in the cloud. The description of the altitude of the cloud base proves to be a key parameter, and accuracy in this regard is vital. This new in-cloud scavenging scheme is intended for use in long-distance (> 100 km) Atmospheric Transport Models (ATMs) or Global Climate Models (GCMs).

Introduction

Clouds are an essential component of the troposphere. They play a central role in meteorological forecasting and in the water cycle on the planet (Zhang *et al*., 2020). Similarly, by interacting with solar radiation, they make a significant contribution to the terrestrial radiation balance (Twomey, 1974; Wang and Su, 2013). Moreover, they are often cited as one of the main sources of uncertainty in climate prediction models (Bony and Dufresne, 2005; Palmer, 2014). They can seriously disrupt air traffic, and even produce aircraft crashes (e. g. Air France flight 447 Rio-Paris air disaster).

By scavenging aerosols, they contribute to improve air quality (Leaitch *et al.*, 1987; Sievering *et al*.,1984), but also to impact soil pollution, through the deposition of atmospheric pollutants via precipitation (Clark and Smith, 1988; Flossmann, 1998). In case of severe nuclear accidents, radioactive aerosol particles might be released into the troposphere (De Cort, 1998 ; Baklanov and Sørensen, 2001 ; Adachi *et al*., 2013). When radionuclides are emitted into the environment, it is essential, in order to protect populations, to jointly assess the concentrations of radioactive aerosols in the atmospheric boundary layer, as well as their transfer to the ground. Thus, during and after the occurrence of an accident, it is necessary to accurately assess the exposures of populations, both by inhalation and by ingestion (Mathieu *et al.,* 2004; Quélo *et al.,* 2007; Quérel *et al.,* 2012).

In nature, deposition of aerosols (and therefore a fortiori of particulate radionuclides) on the ground consists of the contribution of dry deposition and of wet deposition (Slinn 1977). Dry deposition is approximately 1000 times less effective than wet deposition but is the only mechanism operating when there is no precipitation. To date, there are still many uncertainties about the modelling of these two deposition pathways (Petroff *et al.,* 2008, Croft *et al.,* 2010 and Ervens, 2015).

44 Flossmann (1998) used the DESCAM model (Flossmann *et al.,* 1985, 1987, 1988) to assess that, for a droplet from a convective cloud, about 70% of the mass
45 of particles the droplet contains when deposited on the ground was incorporated into the droplet in the cloud. This result is consistent with the
46 measurements in the environment of Laguionie *et al.,* (2014), which estimate the cloud to be 60% responsible for the total downwash of particles.

47 Our objective in this article is to establish theoretically a scavenging coefficient applicable to clouds. Scavenging by clouds is more challenging to model than
48 scavenging by rain, under the cloud, as it is much more sensitive to certain input parameters. Rain scavenging is only controlled by a single microphysical
49 mechanism: collection by raindrops (Kerker and Hampl, 1974; Beard, 1974; Grover *et al.,* 1977; Wang and Pruppacher, 1977; Lai *et al.,* 1978; Pranesha and
50 Kamra, 1996; Vohl *et al.,* 1999; Quérel *et al.,* 2014; Lemaitre *et al.,* 2017), whereas cloud scavenging encompasses a set of mechanisms which will firstly
51 make it possible to incorporate aerosols into the cloud droplets (activation, collection, ice nucleation, collection by crystals) then, secondly, to convert a
52 fraction of the cloud hydrometeors into raindrops (condensation, coalescence, Bergeron effects). Only after raindrops have been deposited on the ground
53 is the atmosphere washed out and, by the same process, the soil contaminated. Furthermore, most atmospheric transport models use significantly different
54 schemes to model scavenging by cloud and by rain. Quérel *et al.,* 2021 summarised a few of them in Table 3 of their article.

55 Therefore, in theoretically assessing cloud scavenging, the use of a cloud formation model such as DESCAM (DEtailed SCAvenging Model), forms a good
56 foundation. This model, developed by Andrea Flossmann and her group since the mid-80s (Flossmann *et al.,* 1985; Flossmann, 1998; Monier *et al.,* 2006;
57 Leroy *et al.,* 2007; Planche *et al.,* 2007; Flossmann and Wobrock, 2010; Hiron and Flossmann, 2015; Dépée, 2019), makes it possible, through a detailed
58 microphysical description, to model clouds from their formation through to precipitation, and to monitor the aerosols and what becomes of them once
59 incorporated into the droplets.

60 In this article, we will show how, using a model like DESCAM, it is possible to theoretically calculate a scavenging coefficient in the cloud, on the scale of the
61 cloud system. We will apply this approach to two extreme types of cloud: a cumulonimbus (CCOPE, Dye *et al.,* 1986) and a stratus (Zhang *et al.,* 2004). This
62 approach will then be compared to the models derived from the deposits observed following the Fukushima nuclear accident (Leadbetter *et al.,* 2015; Quérel
63 *et al.,* 2021). Finally, in the last part we will present, a theoretical scheme of the scavenging coefficient, applicable to any type of cloud, will be proposed.
64 We begin by considering some key elements of the theoretical context and some definitions.

1. Definitions and theoretical context

1.1. Definition of cloud scavenging

67 In large range transport models, the description of scavenging shall remain simple, the operational scientific community models it through a parametrisation
68 involving the cloud scavenging coefficient (Λ_{cloud}). It is defined as the fraction of pollutants that is transferred from the atmosphere to precipitation (then
69 to the ground) per unit of time. In this article, we will focus on pollutants carried by aerosols (and not gaseous pollutants). The scavenging coefficient is
70 therefore defined spectrally thus:

71
$$\frac{dN(d_{ap})}{N(d_{ap})}\bigg|_{cloud} = \frac{dM(d_{ap})}{M(d_{ap})}\bigg|_{cloud} = -\Lambda_{cloud}(d_{ap}).dt \qquad \text{Equation 1}$$

72 In this equation $N(d_{ap})$ and $M(d_{ap})$ are respectively the concentrations in number and in mass of aerosols of diameter d_{ap} per unit of air volume;
73 likewise, $dN(d_{ap})$ and $dM(d_{ap})$ are respectively the variations in concentration in number and in mass of aerosols of diameter d_{ap}, in relation to their
74 transfer into precipitation, per unit of time. The two definitions are considered equal when expressed spectrally, assuming a uniform density of all aerosol
75 particles. In this study, we specifically considered aerosol particles composed of ammonium sulphate, thus confirming this equality. However, in real
76 atmospheric conditions, aerosol particle density is typically not uniform. In such cases, it becomes crucial to specify whether we are referring to a mass
77 scavenging coefficient or a numerical one. To prevent any confusion, in the following article, the exponent m is introduced to the scavenging coefficient
78 Λ_{cloud}^m.

79 The approach we use is to apply this definition to an elementary volume of cloud (volume outlined in red in Figure 1). This volume is bounded at its base by
80 an arbitrary section (dS) aligned with the base of the cloud, with this volume extending vertically to the cloud summit.
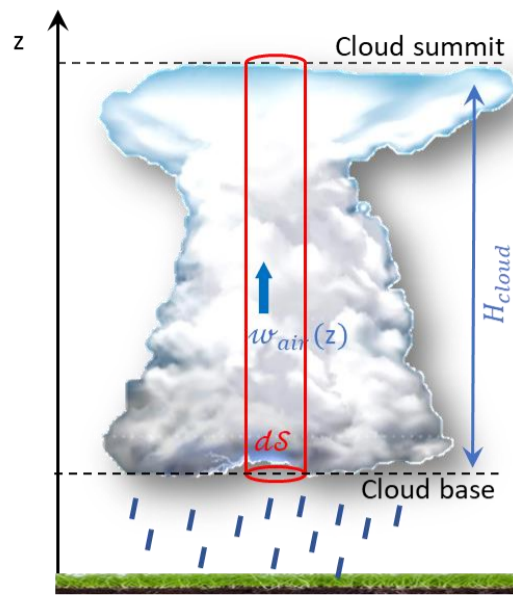
 Figure 1. Definition of the scavenging coefficient at the scale of a cloud

 In this elementary cloud volume, it is elementary to calculate the variation in the average mass concentration of aerosols of diameter d_{ap}, in relation to
 their transfer into precipitation:

$$d\mathcal{M}(d_{ap}) = - \frac{\phi_{ap,precip}(d_{ap}).\,d\mathcal{S}\,.dt}{dV_{cloud}} \qquad \text{Equation 2}$$

 In this equation, $\phi_{ap,precip}(d_{ap})$ is the mass flow of dry particles of diameter (d_{ap}) leaving the cloud via precipitation (solids and liquids), and dV_{cloud} is the
 elementary volume of cloud considered ($dV_{cloud} = H_{cloud}.\,d\mathcal{S}$).

$$\Lambda_{cloud}^{m}(d_{ap}) = -\frac{1}{dt}\frac{d\mathcal{M}(d_{ap})}{\langle\mathcal{M}(d_{ap})\rangle}\bigg|_{cloud} = \frac{\phi_{ap,\ precip}(d_{ap})\big|_{d\mathcal{S}}}{\langle\mathcal{M}(d_{ap})\rangle_{cloud}.\ H_{cloud}} \qquad \text{Equation 3}$$

 In this equation, $\langle\mathcal{M}(d_{ap})\rangle$ is the average mass concentration (over the thickness of the cloud) of dry particles of diameter d_{ap}. It is noteworthy that
 $\langle\mathcal{M}(d_{ap})\rangle$ is not the average concentration of interstitial aerosols in the cloud but the average concentration of particles, which includes, in addition to the
 interstitial aerosols, all the particles included in the droplets and potentially in the ice phase. Thus, if we jointly determine $\langle\mathcal{M}(d_{ap})\rangle$, $\phi_{ap,\ precip}$ as well
 as the thickness of the cloud H_{cloud}, it is possible to deduce a scavenging coefficient.

 The average particle concentration is calculated, using Equation 4, by spatially averaging, over the entire thickness of the cloud, the concentrations of
 interstitial aerosols (of diameters d_{ap}) $\mathcal{M}_{int}(z, d_{ap})$, the concentrations of particles in the drops $\left(\mathbb{M}(z, d_{ap})\right)$, and the concentrations in the ice phase
 $\left(\mathfrak{M}(z, d_{ap})\right)$.

$$\langle\mathcal{M}(d_{ap})\rangle = \frac{1}{H_{cloud}} \int\limits_{cloud\ base}^{cloud\ summit} \left(\mathcal{M}_{int}(z, d_{ap}) + \mathbb{M}(z, d_{ap}) + \mathfrak{M}(z, d_{ap})\right) dz \qquad \text{Equation 4}$$

 Finally, in order to evaluate the mass flow of particles exiting the cloud at its base $\left(\phi_{ap,\ precip}(d_{ap})\right)$, it is necessary to evaluate the cloud volume
 $(\mathcal{V}(\mathcal{D}_{drop}))$ which contains all the droplets whose drop velocity $w_{\infty}(\mathcal{D}_{drop})$ is sufficient for them to pass through the section $d\mathcal{S}$, during the time dt. Using
 the velocity composition law, we can deduce Equation 5.

$$\mathcal{V}(\mathcal{D}_{drop}) = \max\left(0,\ w_{\infty}(\mathcal{D}_{drop}) - w_{air}(\mathcal{Z}_{cloud\ base})\right).d\mathcal{S} \qquad \text{Equation 5}$$

 In this equation, $w_{air}(\mathcal{Z}_{cloud\ base})$ is the velocity of the air parcel at the base of the cloud. By convention, w_{air} is positive for an updraft and negative for
 a downdraft.

 It is then immediately possible to deduce the flow of particles passing $d\mathcal{S}$ through liquid precipitation:

$$\phi_{ap,\ rain}(d_{ap}) = \int_{d_{droplet}=0}^{\infty} \max\left(0,\ w_{\infty}(\mathcal{D}_{drop}) - w_{air}(\mathcal{Z}_{cloud\ base})\right).\mathbb{M}(z, d_{ap}, \mathcal{D}_{drop}).d\mathcal{D}_{drop} \qquad \text{Equation 6}$$

106   In this equation, $\mathbb{M}\left(z, d_{ap}, \mathcal{D}_{drop}\right)$ is the concentration of particles contained in the droplets and of dry diameter d_{ap}.

107   The same applies to solid precipitation $\phi_{ap,\ ice}\left(d_{ap}\right)$:

$$\phi_{ap,\ ice}\left(d_{ap}\right) = \int_{d_{ice}=0}^{\infty} \max(0,\ w_{\infty}(\mathbb{d}_{ice})$$
$$- w_{air}(z_{cloud\ base})).\mathfrak{M}\left(z, d_{ap}, \mathbb{d}_{ice}\right).d\mathbb{d}_{ice}$$

Equation 7

108   By adding these two flows together, it is possible to deduce the total flow of particles (of diameter d_{ap}) exiting the cloud through all precipitation:

109
$$\phi_{ap,\ precip}\left(d_{ap}\right) = \phi_{ap,\ rain}\left(d_{ap}\right) + \phi_{ap,\ ice}\left(d_{ap}\right)$$

Equation 8

110

111   Thus, to theoretically evaluate the cloud scavenging coefficient, it is first and foremost essential to be able to evaluate its contours, but also to be able to

112   determine the mass concentrations of particles in the droplets $\mathbb{M}\left(z, d_{ap}, \mathcal{D}_{drop}\right)$, in the ice phase $\mathfrak{M}(z, \mathbb{d}_{ice}, d_{ap})$, and in the interstitial aerosol $\mathcal{M}_{int}\left(z, d_{ap}\right)$.

113   To evaluate the contours of the cloud, it seems necessary in the first instance to consider once again its definition.

1.2. What is a cloud? (how to define its boundaries?)

115   The World Meteorological Organization defines clouds as: "an aggregation of minute particles of liquid water or ice, or of both, suspended in the atmosphere

116   and usually not touching the ground" (WMO, 2014). This definition would appear to be very inadequate for enabling the contours of a cloud to be

117   determined. Clouds, although very commonly talked about in everyday life and subject to numerous scientific studies, have contours that remain very

118   blurred. It is therefore always difficult to define them rigorously, and above all non-recursively. Spankuch *et al.,* (2022) further emphasised that, depending

119   on the scope of the authors' expertise (meteorology, climate, satellite observations, airborne, from ground radars, or using microphysical models), these

120   authors use significantly differing definitions and thresholds.

121   For example, Wood and Field, 2011 proposed criteria with respect to liquid water content (LWC), ice water content (IWC), or total concentrations in numbers

122   of hydrometeors (droplets and crystals).

123   Hiron (2018) proposed separating cloud water and precipitation water based on the criterion of the size of hydrometeors (hydrometeors with a diameter of

124   less than 64 μm are considered part of the cloud; larger than that are considered part of the rain); then, if the total cloud water content is greater than 0.1

125   g/cm³, the air parcel is considered part of the cloud.

126   Other authors proposed contours based on relative humidity (Del Genio *et al.*, 1996) or total water content (TWC), whereas meteorologists and

127   climatologists tend to prefer optical thickness (Sassen and Cho, 1992), each with arbitrarily established thresholds.

128   Although these definitions can be linked mathematically to each other, these relationships are most often highly non-linear. Therefore, in this article, a

129   variety of cloud definitions will be considered, and we will examine the criteria that are most relevant for studying in-cloud scavenging and distinguishing it

130   from below-cloud scavenging. This relevance of the definition what constitutes a cloud will be analysed from two perspectives. Firstly, we consider a purely

131   physical perspective and, secondly, a more pragmatic perspective linked rather to applicability in an atmospheric dispersion model dedicated to crisis

132   management.

1.3. The DESCAM model

134   To simulate clouds of different types and theoretically evaluate their scavenging coefficient, it is necessary to have a model that makes it possible to simulate

135   all the water phase changes, considering the catalyst role of aerosols in most of these state changes (activation, ice nucleation, etc.). It is also necessary to

136   calculate the sink terms of interstitial aerosols (related to droplet collection or activation) and associate them with the source terms of particles in droplets

137   and ice, in order to calculate the mass of particles in droplets $\left(\mathbb{M}(d_{drop})\right)$ and in ice $\left(\mathfrak{M}(d_{ice})\right)$ throughout the simulation (Equation 6, Equation 7).

138   The DESCAM model meets these specifications. This detailed microphysical model classifies droplets $\left(\mathcal{D}_{drop} \in [1\ \mu m, 6.5\ mm]\right)$, ice $\left(\mathbb{d}_{ice} \in\right.$

139     $[1\ \mu m, 6.5\ mm])$, and aerosols $\left(d_{ap} \in [2\ nm, 12.7\ \mu m]\right)$, each into 39 logarithmically distributed size classes. This makes it possible to explicitly monitor

140   their respective particle size distributions $\mathbb{N}\left(\mathcal{D}_{drop}\right)$, $\mathfrak{R}(\mathbb{d}_{ice})$ and $\mathcal{N}(d_{ap})$, spatially and temporally. This model can be coupled with various dynamic models

141   that allow consideration of atmospheric flows. In this article, we will only consider a dynamic called 1D1/2 (Asai and Kasahara, 1967), implemented in the

142   DESCAM model by Monier, 2003. More realistic 3D dynamics (Clark and Hall, 1991) are implemented in DESCAM (Leroy 2007) but will not be considered in

143   this article.

Description of the microphysical models modelled in DESCAM

145   All the microphysical processes considered in the DESCAM model are presented in Figure 2.
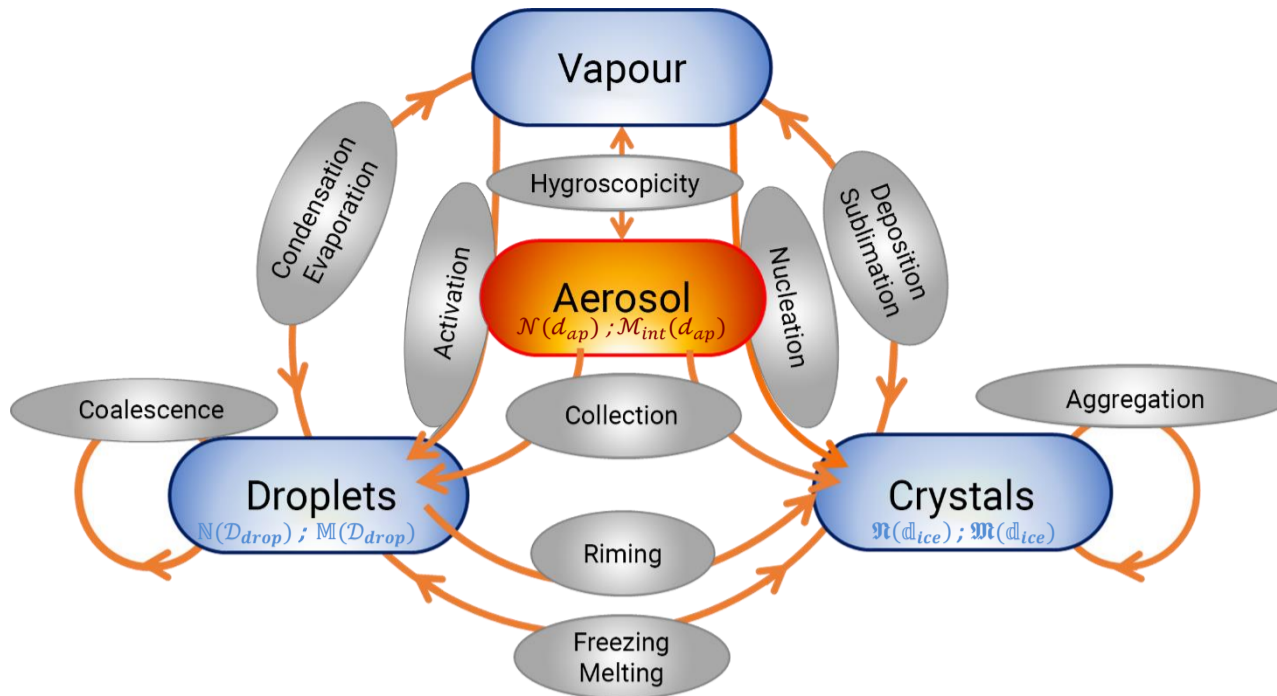
Figure 2. Modelling of microphysical processes in the DESCAM model.

In this figure, we can see the central role of aerosols in most water phase changes. The explicit resolution of all these microprocesses enables calculation of the particle size distributions of aerosols in each grid cell and at each time step (in number: $\mathcal{N}(d_{ap})$ (Equation 9) and in mass: $\mathcal{M}(d_{ap})$),) as well as the particle size distributions of the droplets (in number $\mathbb{N}(\mathcal{D}_{drop})$, Equation 10) and of the ice (in number $\mathfrak{N}(\mathbb{d}_{ice})$, Equation 11). In addition, in order to preserve the total mass of particles, the model also calculates two other quantities that are used to determine the masses of particles in droplets of diameter d_{drop} $\left(\mathbb{M}(\mathcal{D}_{drop})\right)$, and in ice crystals of diameter d_{ice} $\left(\mathfrak{M}(\mathbb{d}_{ice})\right)$.

$$\frac{d\mathcal{N}(d_{ap})}{dt} = \frac{d\mathcal{N}(d_{ap})}{dt}\bigg|_{dyn} + \frac{d\mathcal{N}(d_{ap})}{dt}\bigg|_{co\ell\ell} + \frac{d\mathcal{N}(d_{ap})}{dt}\bigg|_{hygro} + \frac{d\mathcal{N}(d_{ap})}{dt}\bigg|_{act,\ deact} \qquad \text{Equation 9}$$

$$\frac{d\mathbb{N}(\mathcal{D}_{drop})}{dt} = \frac{d\mathbb{N}(\mathcal{D}_{drop})}{dt}\bigg|_{dyn} + \frac{d\mathbb{N}(\mathcal{D}_{drop})}{dt}\bigg|_{act,\ deact} + \frac{d\mathbb{N}(\mathcal{D}_{drop})}{dt}\bigg|_{coal}$$
$$+ \frac{d\mathbb{N}(\mathcal{D}_{drop})}{dt}\bigg|_{cond,\ vap} + \frac{d\mathbb{N}(\mathcal{D}_{drop})}{dt}\bigg|_{riming} + \frac{d\mathbb{N}(\mathcal{D}_{drop})}{dt}\bigg|_{frz,\ melt} \qquad \text{Equation 10}$$

$$\frac{d\mathfrak{N}(\mathbb{d}_{ice})}{dt} = \frac{d\mathfrak{N}(\mathbb{d}_{ice})}{dt}\bigg|_{dyn} + \frac{d\mathfrak{N}(\mathbb{d}_{ice})}{dt}\bigg|_{nucleation} + \frac{d\mathfrak{N}(\mathbb{d}_{ice})}{dt}\bigg|_{frz,\ sub} + \frac{d\mathfrak{N}(\mathbb{d}_{ice})}{dt}\bigg|_{agg}$$
$$+ \frac{d\mathfrak{N}(\mathbb{d}_{ice})}{dt}\bigg|_{riming} + \frac{d\mathbb{N}(\mathbb{d}_{ice})}{dt}\bigg|_{frz,\ melt} \qquad \text{Equation 11}$$

$$\frac{d\mathbb{M}(\mathcal{D}_{drop})}{dt} = \frac{d\mathbb{M}(\mathcal{D}_{drop})}{dt}\bigg|_{dyn} + \frac{d\mathbb{M}(\mathcal{D}_{drop})}{dt}\bigg|_{act,\ deact} + \frac{d\mathbb{M}(\mathcal{D}_{drop})}{dt}\bigg|_{coal}$$
$$+ \frac{d\mathbb{M}(\mathcal{D}_{drop})}{dt}\bigg|_{cond,\ vap} + \frac{d\mathbb{M}(\mathcal{D}_{drop})}{dt}\bigg|_{riming} + \frac{d\mathbb{M}(\mathcal{D}_{drop})}{dt}\bigg|_{frz,\ melt} \qquad \text{Equation 12}$$

$$\frac{d\,\mathfrak{M}(\mathbb{d}_{ice})}{dt} = \frac{d\,\mathfrak{M}(\mathbb{d}_{ice})}{dt}\bigg|_{dyn} + \frac{d\,\mathfrak{M}(\mathbb{d}_{ice})}{dt}\bigg|_{nucleation} + \frac{d\,\mathfrak{M}(\mathbb{d}_{ice})}{dt}\bigg|_{frz,\ sub} + \frac{d\,\mathfrak{M}(\mathbb{d}_{ice})}{dt}\bigg|_{agg}$$
$$+ \frac{d\,\mathfrak{M}(\mathbb{d}_{ice})}{dt}\bigg|_{riming} + \frac{d\,\mathfrak{M}(\mathbb{d}_{ice})}{dt}\bigg|_{frz,\ melt} \qquad \text{Equation 13}$$

In these equations, except for the index $\left(\ \big|_{dyn}\right)$ denoting variations due to atmospheric transport, each term corresponds to one of the microphysical processes outlined in Figure 2. For instance, $\left(\ \big|_{act,\ deact}\right)$ denotes to activation and deactivation processes. The subscripts $co\ell\ell,\ hygro,\ frz,\ sub,\ coal,$ $cond,\ vap$ and agg respectively refers to the processes of aerosol collection by droplets, hygroscopicity of aerosol particles, freezing, sublimation,

163 coalescence, condensation, vaporization, and aggregation. The hygroscopic growth of aerosol particles is calculated assuming they are in thermodynamic

164 equilibrium with the air supersaturation S (Equation 14). This equilibrium is modelled after the κ-Köhler theory.

$$\frac{dN(d_{ap})}{dt}\bigg|_{hygro} = \frac{\partial N(d_{ap})}{\partial S}\bigg|_{\kappa-K\ddot{o}hler} \frac{\partial S}{\partial t}\bigg|_{dyn} \qquad \text{Equation 14}$$

165

166 Concerning the cold microphysics (Figure 2), this simulation integrates homogeneous freezing mechanisms (i.e., which do not require aerosol contribution)

167 and heterogeneous freezing mechanisms (for which aerosols act as a catalyst for phase change). For homogeneous freezing, we consider the parametrisation

168 of Koop *et al.,* (2000) adapted to DESCAM by Monier *et al.,* (2006). To model heterogeneous ice nucleation, we consider all the mechanisms described by

169 Vali *et al.,* (2015). The Biggs formula (1953) is used to describe immersion freezing and the model of Meyers *et al.,* (1992) for condensation and contact

170 freezing, as well as deposition nucleation. All these mechanisms have recently been incorporated into the DESCAM model by Hiron and Flossmann, (2015).

171 The main mechanism responsible for the flow of particles exiting the cloud via precipitation ($\phi_{ap,\ precip}(d_{ap})$, Equation 3) is activation. The collection of

172 aerosols by droplets is only second order (Flossmann and Wobrock, 2010; Dépée, 2019). In the DESCAM model, activation is modelled by the κ-Köhler theory

173 (Petters and Kreidenweis, 2007). This model makes it possible to determine equilibrium vapour pressure in the vicinity of a droplet of diameter $\mathcal{D}_{drop}$, as a

174 function of the mass and type of solute (modelled by the κ value) it contains, and therefore the supersaturation for this droplet. For a given mass and

175 chemical nature of the pristine dry particle, one can compute the corresponding supersaturations for given size of solution droplets. This curve has a unique

176 maximum, called critical supersaturation (Figure 3). The diameter associated with this critical supersaturation is called the activation diameter. Aerosols

177 with a diameter smaller than the activation diameter are brought into thermodynamic equilibrium with their environment by hygroscopicity, with aerosols

178 of a diameter greater than the activation diameter being converted into droplets and growing by means of vapour diffusion (by condensation).

179 In the DESCAM code, the microphysical process of collection (i.e. the process by which, during falling, droplets encounter impact and capture interstitial

180 aerosol particles), is modelled in Equation 12 by the term $\frac{d\mathbb{M}(\mathcal{D}_{drop})}{dt}\big|_{coll}$ which is calculated by solving Equation 15. In this equation, the central term is the

181 collection efficiencies $\left(E(d_{ap}, \mathcal{D}_{drop}, \mathcal{RH})\right)$. This is calculated by the model developed and validated by Dépée (Dépée *et al*., 2019; Dépée *et al*., 2021, Part I;

182 Dépée *et al*., 2020, Part II).

$$\frac{d\mathbb{M}(\mathcal{D}_{drop})}{dt}\bigg|_{coll} = \int_{d_{ap}=0}^{\infty} N(d_{ap}) \frac{\pi \mathcal{D}_{drop}^2}{4} \mathcal{U}_{\infty,\ droplet}(\mathcal{D}_{drop}) E(d_{ap}, \mathcal{D}_{drop}, \mathcal{RH}) \frac{\pi d_{ap}^3}{6} \rho_{ap} \ dd_{ap} \qquad \text{Equation 15}$$

183 In this equation $\mathcal{U}_{\infty,\ droplet}(\mathcal{D}_{drop})$ corresponds to the terminal velocity of a droplet of diameter $\mathcal{D}_{drop}$ (calculated after the Beard (1973) model), ρ_{ap} is

184 the density of the aerosol particle, and $\mathcal{RH}$ refers to the relative humidity of air in the parcel.

185
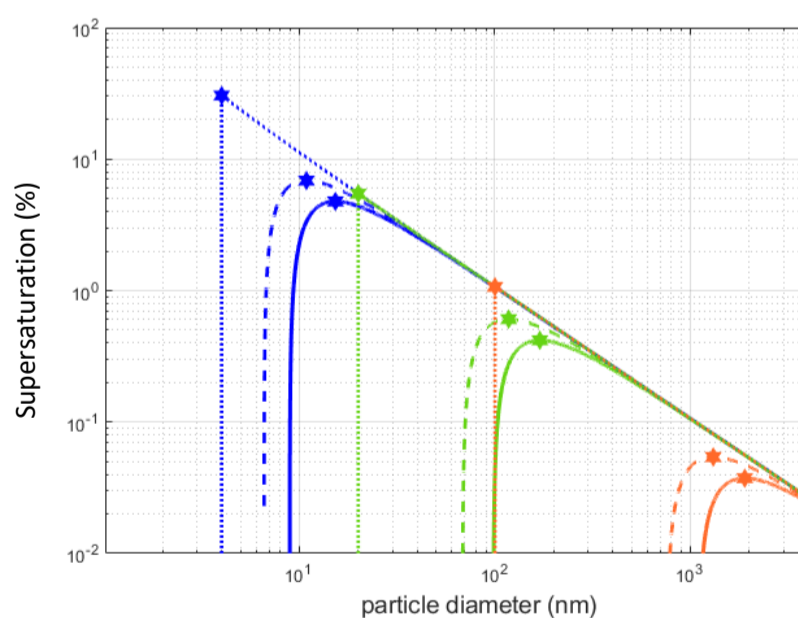
187 Figure 3. Thermodynamic equilibrium of an aerosol calculated as a function of particle diameter and nature of the initial dry particle. This
188 calculation is made using the κ-Köhler theory (for a temperature of 293 K and a surface tension between solution and air of 72 × 10^{-3} N.m^{-1}).
189 (—) initial dry radius of the particles set at 4 nm; (—) initial dry radius set at 20 nm; (—) initial dry radius set at 100 nm;
190 (⋯) κ = 0, insoluble aerosol; (--) κ = 0.61, moderately hygroscopic, as (NH$_4$)$_2$SO$_4$; (—) κ = 1.28, highly hygroscopic, as NaCl;
191 ✷ critical supersaturations needed to activate the aerosol and convert it into a cloud droplet.

192

193 Note that Equation 6 and Equation 7 are not directly calculable by the DESCAM model. This is because the model makes an inventory of the mass of particles

194 in the droplets and crystals according to the size of the hydrometeors ($\mathbb{M}(\mathcal{D}_{drop})$, Equation 12 and $\mathfrak{M}(\mathbb{d}_{ice})$, Equation 13), but without memorising the size

195 of the aerosols before their incorporation. The scavenging coefficients calculated in this article are therefore averaged, in mass, over the particle size

196 distribution of the aerosols. In this article we focus on validating the approach described by applying it to different types of cloud. Current work and future

197 publications will focus on demonstrating that the scavenging coefficient may be simply spectrally calculated, without modifying the model.

198

Modelling of atmospheric dynamics

200 As stated previously, in this article we have limited our study to the 1.5D Dynamic framework developed by Asai and Kasahara, (1967). This has been regularly

201 used (Monier *et al*., 2005; Leroy *et al.,* 2006; Quérel *et al*., 2014; Hiron & Flossmann, 2015) to study the microphysical processes involved in the life cycle of

202 cumulus clouds. This model considers two concentric cylinders. The inner cylinder has a radius 10 times smaller than the outer cylinder. In the inner cylinder,

203 the vertical velocity of the flows is determined by solving a simplified form of the Navier-Stokes equations, coupled with the energy conservation equation.

204 The outer cylinder serves primarily for guaranteeing the condition of zero velocity divergence (continuity equation for incompressible flow). To this end, a

205 radial velocity component is introduced at the interface between these two cylinders (hence the expression of a 1.5D model), calculated from the

206 convergence or divergence layers and allowing entrainment from the environment. In this environment the only variable updated in this outer cylinder is

207 the vertical velocity to evaluate the radial gradient in vertical velocity and the subsequent turbulent flux; all the other variables are assumed to be unaffected

208 by the cloud processes within the inner cylinder and kept constant throughout the simulation.

209 All the microphysical processes detailed in the previous section and summarised in Figure 2 are calculated only in the central cylinder. Thus, this is also in

210 the inner cylinder, for each grid layer, that phase changes in the water will be computed with the subsequent absorption or release of latent heat that will

211 alter the buoyancy of the air and which ultimately generate the updraft and downdraft motions.

2. Application to example cloud types

213 To establish a theoretical scavenging coefficient scheme, the methodology described above is applied to two very different idealised case studies

214 representative of two different types of clouds. First, we will model a vigorous cumulonimbus, then a shallow stratus. These two cloud types were selected

215 as they present, respectively, the higher and lower values, in terms of vertical extension, relative humidity, and rainfall intensity. Furthermore, while the

216 stratus that we simulate is thin and low altitude enough to be a warm cloud, cold microphysical processes are essential to capture the development of the

217 cumulonimbus situation.

218

2.1. Application to a cumulonimbus

Description of the cumulonimbus considered

221 The cloud selected to model the cumulonimbus is the episode of 19 July 1981 of the CCOPE campaign (Cooperative Convective Precipitation Experiment;

222 Knight 1982 and Dye *et al.,* 1986), which took place near Miles City in Montana (USA). This episode was selected because it is very finely documented and

223 this episode is a test case for many codes simulating the formation of convective clouds, and in particular the DESCAM model (Flossmann & Wobrock, 2010).

224 A radio sounding taken at Miles City at 16h00 local time (just before the storm) is used to initialise the thermodynamic conditions of the atmospheric column:

225 temperature and humidity. For the vertical pressure profiles, standard conditions are assumed. In addition, we used the observations of both two Doppler

226 radars measured high-resolution reflectivity as well as the movements of the cloud and five aircrafts that were able to make numerous passes through the

227 cloud throughout its maturation and through to the precipitation episodes. The spatial-temporal evolution of the thermodynamic conditions, associated

228 with the microphysical properties of the cloud system, and the atmospheric flows are therefore recorded in fine detail for the entire life of this cumulonimbus

229 and can be used to evaluate the model performance to capture the clouds physics. For this article, we therefore used the same modelling hypotheses as

230 those detailed by Leroy *et al.,* (2006). Convection was triggered by +2.3°C heating of the ground during the first 10 minutes of the simulation. During this

231 campaign, no physicochemical measurements were made of the aerosols, hence we consider that they consisted of ammonium sulfate ($\kappa = 0.61$ and $\rho_{dry} =$

232 1.77×10^3 kg.m^{-3} Petters and Kreidenweis, 2007) with an initial particle size distribution of the Jaenicke continental type (1988). We considered a homogeneous

233 distribution in the atmospheric boundary layer (i.e., over the first 3 kilometres), then above the concentration is assumed to decrease exponentially with a

234 scale height of 3000 m (Figure 4).

235
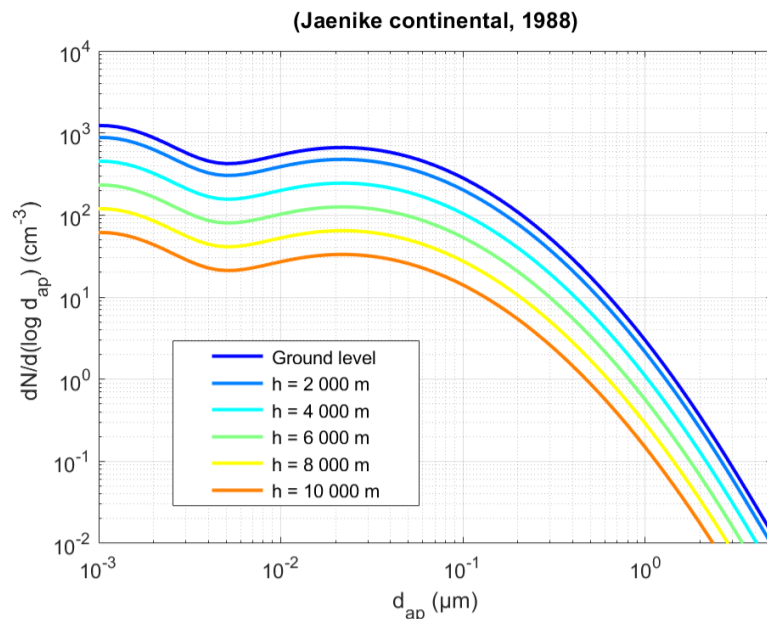
236   Figure 4. Initial particle size distribution of aerosols considered for this simulation.

237   The simulation lasted 3600 s, on a 10 km high column. The spatial and temporal resolutions were set to 100 m and three seconds respectively.

238   Figure 5 and Figure 6 show respectively the spatial-temporal evolutions of the vertical flows in the central cylinder and the liquid water and ice content.

239
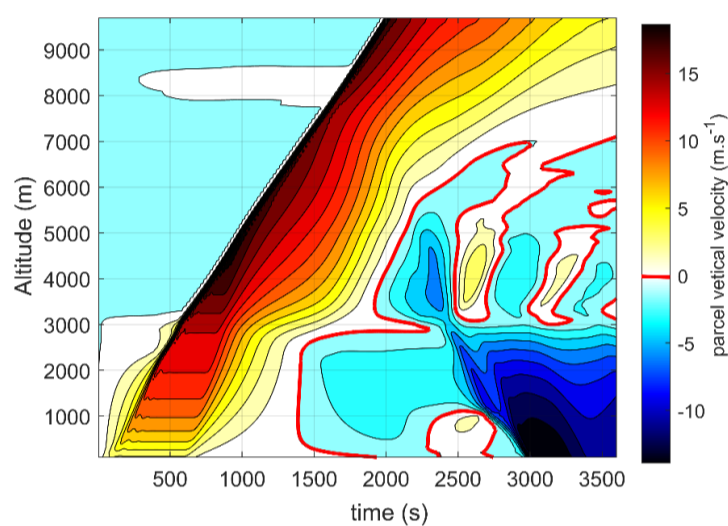
240   Figure 5. Spatial-temporal distribution of the vertical components of atmospheric flows. The thick line in red separates the updraft ($w_{air} > 0$) flows from
241   the downdraft flows ($w_{air} < 0$).

242   In these figures, we can see that the initial superheating of the air layer at ground level induces an updraft flow due to buoyancy forces. Approximately 500 s
243   after the start of the simulation, the air reaches critical supersaturation at an altitude of 3000 m and the aerosols are gradually converted into droplets. The
244   spatial-temporal distribution shown on the left of Figure 6 highlights the appearance of a cloud at the spatial-temporal coordinate (500 s, 3000 m). Vapour
245   condensation induces a latent heat release, which in turn increases buoyancy of the air parcel, accelerating the updraft flows (approx. 15 m.s^{-1} at 4000 m).
246   This flow transports the vapour at altitude and by cooling this induces the progressive activation of the aerosols, and a vertical extension of the cloud. Near
247   7000 m, the first ice crystals are formed. The coexistence of ice crystals and supercooled droplets will allow rapid crystal growth with a corresponding
248   reduction of liquid water content (best known as the WBF process for: Wegener, 1911; Bergeron, 1928; Findeisen, 1938). Then, the crystals begin to
249   precipitate at around 1700 s since they reach sizes large enough for their gravitational settling velocity to supersede updraft speed. In precipitating, the
250   larger crystals collect the suspended droplets. Hence, under the coupled influence of the WBF process and, above all, the collection of droplets by the ice
251   particles, after 2200 seconds of simulation the cloud only contains ice. Finally, below an altitude of 3000 m, the solid hydrometeors melt and liquid
252   precipitation forms. Figure 6 shows on the right the rainfall intensities, as well as the cumulative precipitation calculated by the model at ground level. This
253   timeline presents two local maxima: the first at 2750 s after the start of the simulation, corresponding to an intensity of 18 mm.h^{-1} and the second 300 s
254   later, with an intensity of about 46 mm.h^{-1}.

255
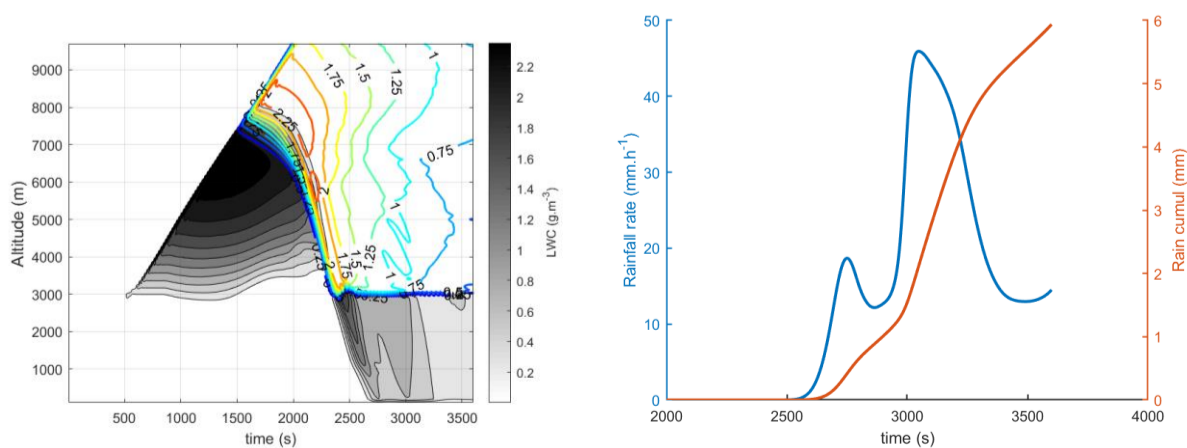
256   Figure 6. On the left: Spatial-temporal distributions of liquid water content (LWC, greyscale) and ice content (IWC, iso-contours).
257   On the right: Temporal evolution of rainfall intensity and cumulative precipitation at ground level

Calculation of the scavenging coefficient

258

259 Based on this modelling results, we applied all the methodology described in section 1.1. The first step consisted in establishing the contours of the cloud,

260 in order then, using Equation 3 integrated over the entire aerosol distribution, to be able to calculate the equivalent cloud scavenging coefficient.

$$\Lambda_{cloud}^{m} = -\frac{1}{dt}\frac{d\mathcal{M}}{\langle\mathcal{M}\rangle}\bigg|_{cloud} = \frac{\phi_{ap,\ precip}}{\langle\mathcal{M}\rangle\cdot H_{cloud}} \qquad\qquad \text{Equation 16}$$

261 As already indicated in section 1.2, there is no strict definition of the boundaries of the cloud, particularly at the interface with the precipitation, and it can

262 also be observed in Figure 6 that the total water content does not show any demarcation between the cloud and the precipitation. Moreover, as Spänkuch

263 *et al.*, (2022) point out, the physical phenomenon studied will determine which contours are the most relevant. Therefore, for this study, we examined three

264 of the physical parameters to establish this contour. These three criteria are the relative humidity of the air parcel (calculated in relation to liquid water),

265 the mass concentration of hydrometeors with a diameter of less than 64 µm and, lastly, the concentration of hydrometeors. The contours of this

266 cumulonimbus are presented in Figure 7 for each of these criteria, each with two thresholds considered.
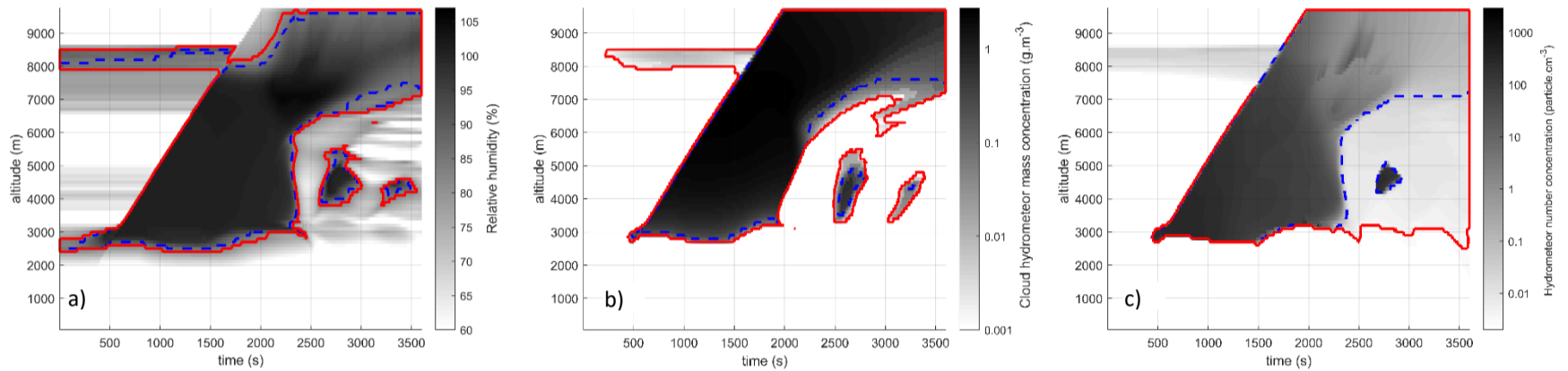
267

268 Figure 7. Test of different criteria to establish the contours of the simulated cumulonimbus.

269 a) threshold based on relative humidity: (- - -) $RH > 85\%$; (—) $RH > 80\%$.

270 b) threshold based on the total water content of hydrometeors with a diameter less than 64 µm: (- - -) mass concentration of cloud

271 hydrometeors $> 0.1\ g.m^{-3}$; (—) mass concentration of cloud hydrometeors$> 0.001 g.m^{-3}$.

272 c) threshold based on number concentration of total hydrometeors: (- - -) $\int d\mathbb{N} + d\mathfrak{R} > 0.03\ cm^{-3}$

273 (—) $\int d\mathbb{N} + d\mathfrak{R} > 0.003\ cm^{-3}$

274 We can see in this figure that, apart from the criterion based on the concentration of hydrometeors (Equation 9), with a threshold of 0.003 hydrometeors

275 per cubic centimetre, all the other criteria yield very similar contours. Thus, the cloud forms close to an altitude of 3000 m and its base remains constant for

276 up to 2500 s of simulation. During these 2500 s, the cloud thickens vertically until it reaches the tropopause (considered to be at 10,000 m in this calculation).

277 As shown in Figure 6 (on the right), 2500 s corresponds to the start of precipitation. This moment corresponds to an elevation of the base of the cloud up to

278 about 7000 m, except for the last criterion ($\mathcal{N}_{hydrometeor} > 0.003\ cm^{-3}$), for which the height of the base of the cloud remains constant close to the

279 altitude of 3000 m, even during rain.

280 Initially, our objective was to find a bijective relationship between a set of meteorological parameters available in DESCAM and the scavenging coefficient

281 calculated by this methodology. Most often in the literature, cloud scavenging is described as a power function of precipitation intensity (Hertel *et al.*, 1995;

282 MRI, 2015; Leadbetter *et al.*, 2015; Groell *et al.*, 2014; Quérel *et al.*, 2021). Figure 8, Figure 9 and Figure 10 respectively present the contours of the cloud

283 established on the basis of the three criteria previously introduced (Figure 7). Within these contours, we calculated the total mass concentration of

284 ammonium sulfate ($\mathcal{M}(z)$), adding together the respective concentrations of the aerosol phases $(\mathcal{M}_{int}(z))$, in the droplets $(\mathbb{M}(z))$ and in the crystals

285 $(\mathfrak{M}(z))$. Knowing the flux of ammonium sulfate that is within the precipitative hydrometeors through the base of the cloud (Equation 6, Equation 7 and

286 Equation 8), we could deduce the scavenging coefficient, which we plotted according to the precipitation intensity calculated at the base of the cloud. Like

287 Costa *et al.*, (2010), Stephan *et al.*, (2008) and Quérel *et al.* (2021), a threshold of 0.1 mm.h $^{-1}$ was considered to limit noise. In Figure 8, 9, 10, the

288 correspondence of the dots can be deduced with the colour codes of the points. On the left-hand side, the identification of the spatial-temporal coordinates

289 where precipitation and scavenging coefficient are calculated is plotted. On the right-hand side, the corresponding relationship between scavenging

290 coefficient and precipitation intensity can be read. These results are of great importance because they show that the relationship between the scavenging

291 coefficient and the rainfall intensity is the same at the beginning and the end of the rainfall episode. In addition, an adjustment by a power law is determined

292 for each contour. The coefficients for these adjustments are shown in Table 1.

293
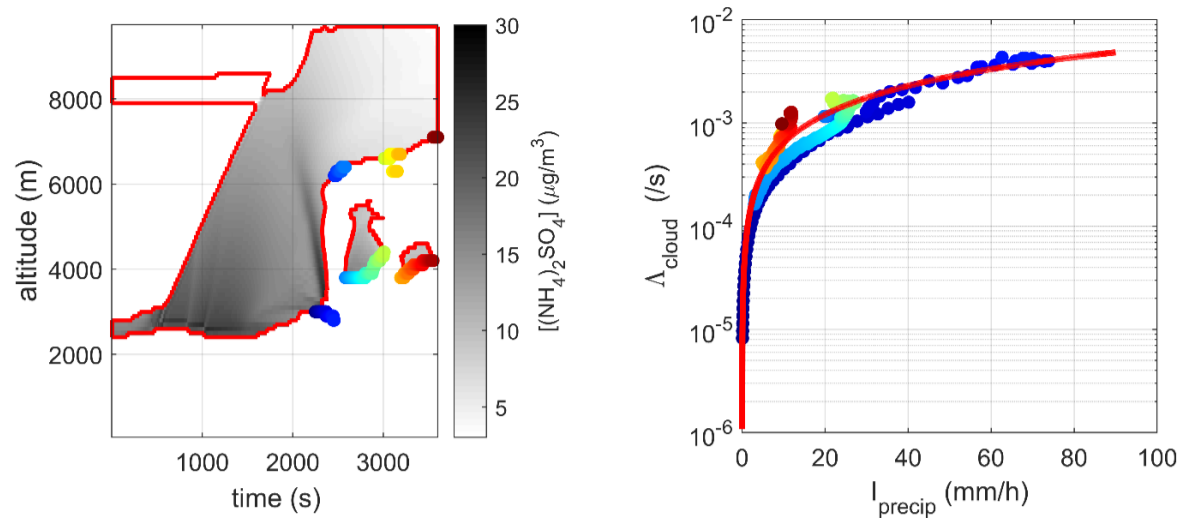
Figure 8. On the left: spatial-temporal distribution of the ammonium sulfate concentration in the cloud contour (—cloud contour for a relative humidity greater than 80%). On the right: correlation between the scavenging coefficient and the precipitation intensity determined at the base of the cloud, (—) adjusted by a power law. Coloured points indicated where and when the scavenging coefficient is calculated, colours are time increasing from the start (blue) to the end (red) of the rainfall.

298
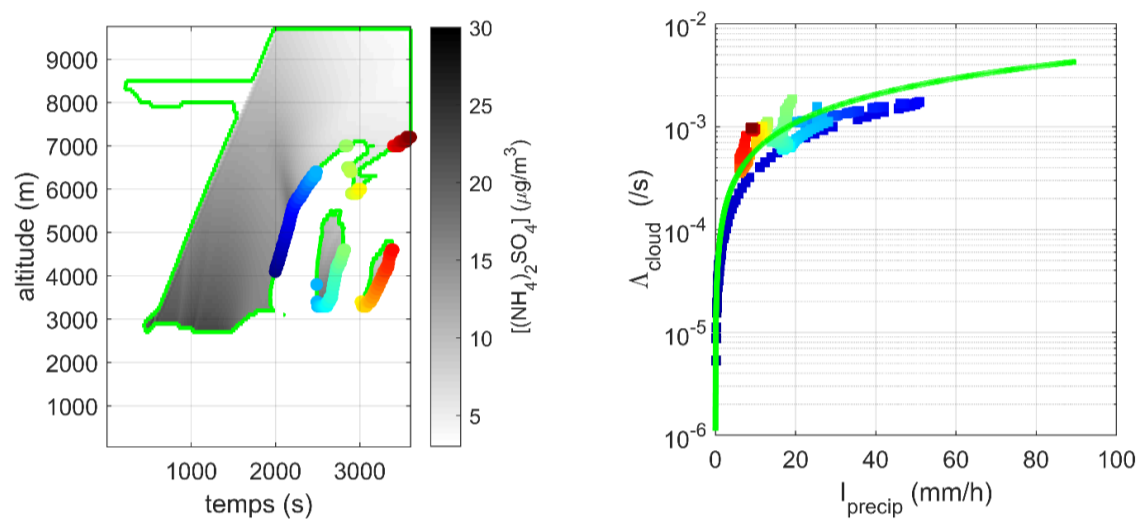
Figure 9. On the left: spatial-temporal distribution of the ammonium sulfate concentration in the cloud contour (— cloud contour for a mass concentration of cloud hydrometeors greater than 0.001 g.m^{-3}). On the right: correlation between the scavenging coefficient and the precipitation intensity determined at the base of the cloud, (—) adjusted by a power law. Coloured points indicated where and when the scavenging coefficient is calculated, colours are time increasing from the start (blue) to the end (red) of the rainfall.

303
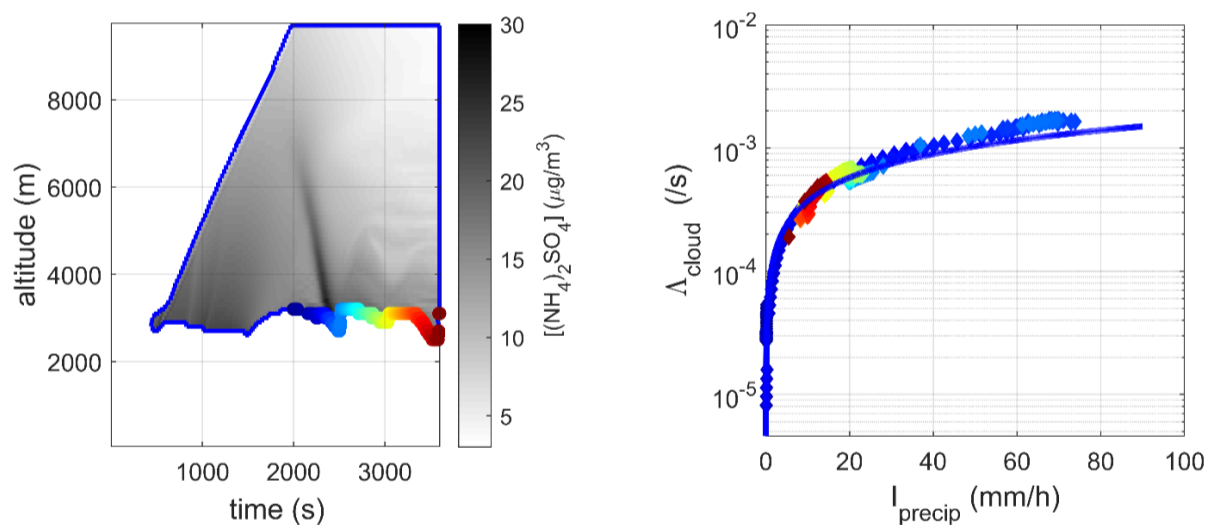
Figure 10. On the left: spatial-temporal distribution of the ammonium sulfate concentration in the cloud contour (— cloud contour for a concentration in number of hydrometeors greater than 0.003 particles.cm^{-3}). On the right: correlation between the scavenging coefficient and the precipitation intensity determined at the base of the cloud, (—) adjusted by a power law. Coloured points indicated where and when the scavenging coefficient is calculated, colours are time increasing from the start (blue) to the end (red) of the rainfall.

308

In these three figures, we observe that the relationship linking the intensity of precipitation to the scavenging coefficient by the cloud is fairly insensitive to the definition selected to describe its contour. Moreover, the power law adjustments plotted in Figure 8, Figure 9 and Figure 10 are very similar (Table 1). Nevertheless, only the last contour, based on the hydrometeor concentration (and with a threshold of 0.003 cm^{-3}), gives a perfectly bijective relationship between the precipitation intensity at the base of the defined contour and the scavenging coefficient. This result is surprising because, as previously mentioned in section 1.3, the driving mechanism for in-cloud scavenging is dominated by the activation (which is driven by the supersaturation level and physical-chemical properties of the aerosols, Flossmann and Wobrock, 2010). It would therefore seem logical that a criterion based on the relative humidity in the grid cell would be the most relevant. However, it is the criterion based on the concentration of hydrometeors that is the more reliable. This is because there are zones in the cloud where the humidity is too low to activate the aerosols (e.g., at 4000 m at 2500 s where RH <85%, or indeed Figure 7a), but where there is a significant number of droplets and crystals (> 0.03 cm^{-3}). These droplets and crystals have been activated elsewhere and previously, but

318 they nevertheless continue to collect aerosols around them – for example by Brownian capture, contributing to scavenging. It therefore justifiable to define

319 a cloud contour based on a diagnostic of the numeric concentration of hydrometeors.

320

321 Table 1: Power law adjustment associated with each of the cloud contours studied.

Contour type	Power law adjustments
Based on relative humidity **(Figure 8)**	$\Lambda_{cloud}^m = 7.6 \times 10^{-5} I^{0.92}$
Based on mass concentration of cloud **hydrometeors** **(Figure 9)**	$\Lambda_{cloud}^m = 7.2 \times 10^{-5} I^{0.9}$
Based on numeric concentration of **hydrometeors** **(Figure 10)**	$\Lambda_{cloud}^m = 8.6 \times 10^{-5} I^{0.6}$

322

323 However, this numeric concentration criterion, although more precise for theoretically assessing the scavenging coefficient, is not easily accessible in a crisis

324 code. Nevertheless, detailed analysis of the results of these simulations seems to show that it would be wise to define the cloud base as being constant and

325 equal to the altitude at which critical supersaturation was first reached, i.e., the altitude at which the cloud began its formation.

326

2.2. Application to a stratus

Description of the stratus considered

329 The same approach as above was considered for modelling scavenging by a shallow stratus cloud. The main differences with the previous modelling (i.e., of

330 the cumulonimbus) beyond the initialisation of thermodynamical profile is the treatment of the vertical advection within the cloud. Whereas, for the

331 previous modelling, differences in air buoyancy (related to the initial thermal gradients and latent heat released by water phase changes) were the cause of

332 vertical velocities and could be described and captured by the dynamics of the model. When it comes to modelling stratus clouds, the dynamics are governed

333 by large scales features that are not included in the 1.5D model. Therefore, the idea is to completely prescribe the time evolving profile for vertical velocity

334 to model this forcing. Since convection is forced rather than triggered by buoyancy, it's reasonable to prescribe it and not calculate the microphysical

335 feedback on dynamics. For the scenario, we considered the vertical advection model proposed by Zhang *et al.,* (2004) and recapitulated in Equation 17. We

336 therefore imposed a sinusoidal profile vertical velocity, the maximum oscillating from positive to negative values with a period of 1800 s. The maximum of

337 the velocities was located at the altitude (z_c) of 1000 m and vertical motions allowed between 700 and 1300 m (h$_c$ = 600 m, Figure 11). Like Zhang *et al.,*

338 (2014), in the advection model, we imposed an average updraft velocity (w_0) of 0.2 m.s^{-1} and an oscillation amplitude (w_1) of 0.8 m.s^{-1} at an altitude of

339 1000 m. Figure 5 shows the spatial-temporal distribution of vertical flows prescribed in the central cylinder. The temperature profile follows a dry adiabatic

340 lapse rate with a temperature of 15°C on the ground so that there are no negative temperatures in the cloud. Above 1300 m, like Zhang *et al.* (2014), we

341 imposed an inversion of the thermal profile. At altitudes between 700 and 1300 m, the relative humidity was initialised at 98.5%, and 95% outside of this

342 range. For the aerosols, the initial conditions were identical to those for cumulonimbus (Equation 5).

$$\begin{cases} w(z,t) = \cos\left(\pi \frac{z - z_c}{h_c}\right)\left[w_0 + w_1 \sin\left(\frac{2\pi t}{t_c}\right)\right] & if \ |z - z_c| \leq \frac{h_c}{2} \\ w(z,t) = 0 & if \ |z - z_c| > \frac{h_c}{2} \\ z_c = 1000 \ m; \ h_c = 600 \ m; \ t_c = 1800 \ s; \ w_0 = 0.2 \ m.s^{-1}; w_1 = 0.8 \ m.s^{-1} \end{cases}$$

Equation 17

343
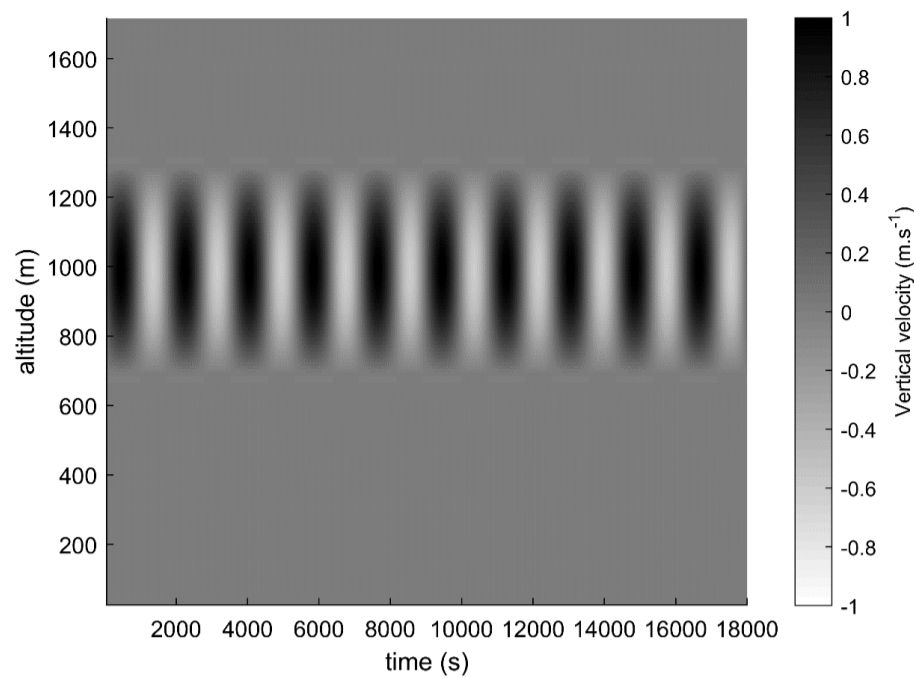
Figure 11. Spatial-temporal distribution of the vertical components of atmospheric flows (Zhang *et al.*, 2004)

345 Figure 12 shows on the left the spatial-temporal distribution of the water content calculated by DESCAM. The critical supersaturation was reached close to

346 the altitude of 700 m from the first updraft phase (0–1000 s). The LWC then increased with altitude throughout the phase where the atmospheric flows

347 were ascending. At the cloud summit, the liquid water content reached approximately 1.6 g.m^{-3}. Conversely, during the downdraft phases, the supply of dry

348 air to lower altitudes induced, due to the temperature profile considered, a drop in the relative humidity occurs, which in turn induced evaporation of the

349 droplets, resulting in a significant reduction in the LWC. These downdraft phases also had the effect of advecting droplets below the cloud band. During the

350 period of velocity oscillations ($t < t_c$), precipitation completely evaporated before reaching the ground. However, from the second period onwards, rain

351 was diagnosed at ground level (Figure 6. b).
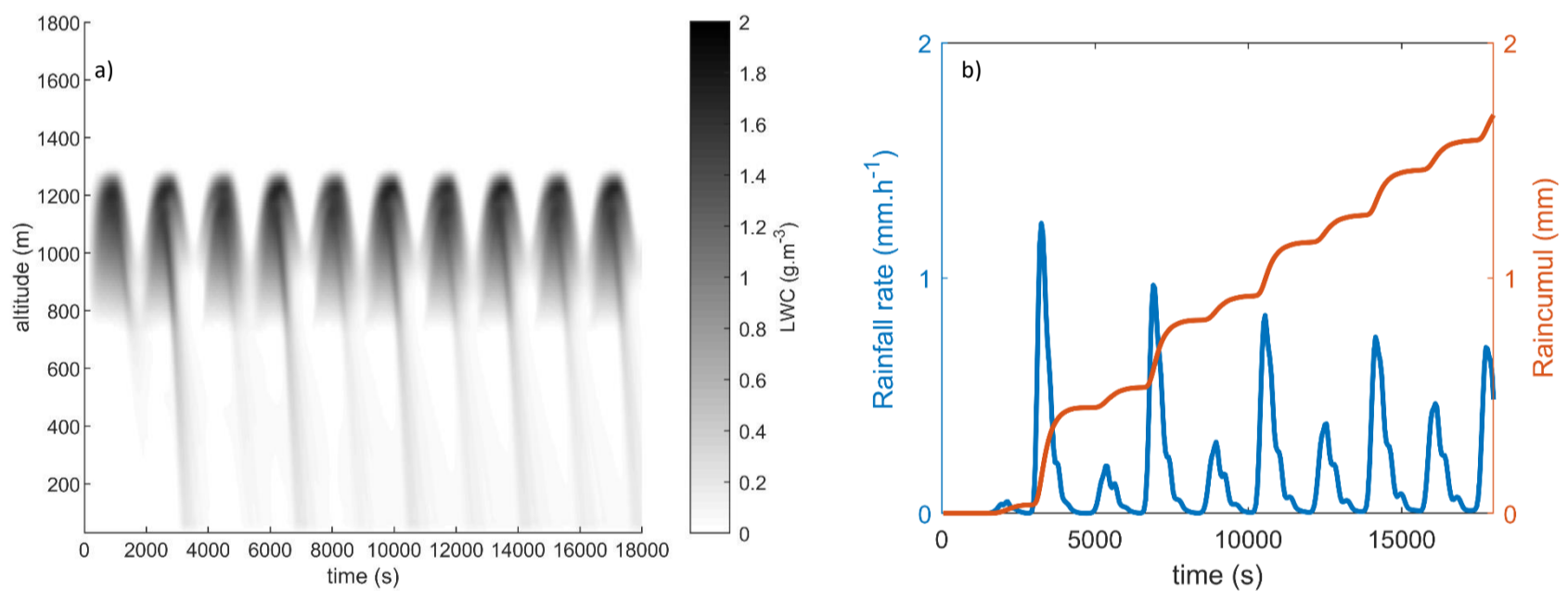
352

353 Figure 12. On the left: Spatial-temporal distribution of the liquid water content calculated by DESCAM (LWC, in greyscale).
354 On the right: Temporal evolution of rainfall intensity and cumulative precipitation diagnosed by DESCAM at ground level.

355 The DESCAM model predicts intermittent precipitation at ground level with flurries of precipitation in the order of a millimetre per hour. Over a precipitation

356 period of approximately four hours, the cumulative precipitation was only approximately 3 mm.

357

358 **Calculation of the stratus scavenging coefficient**

359 As before in the case of cumulonimbus, it is necessary to define the contours of the cloud. We therefore used the three criteria previously introduced and

360 look for the one with the clearest demarcation line between the cloud zone and the precipitation zone, to apply a dedicated scavenging coefficient (Figure

361 13). As before, we observe from Figure 12.a that water content is not a good indicator to outline the cloud boundaries. Indeed, no discontinuity is observed

362 for this parameter enabling demarcation between the cloud and the precipitation.

363
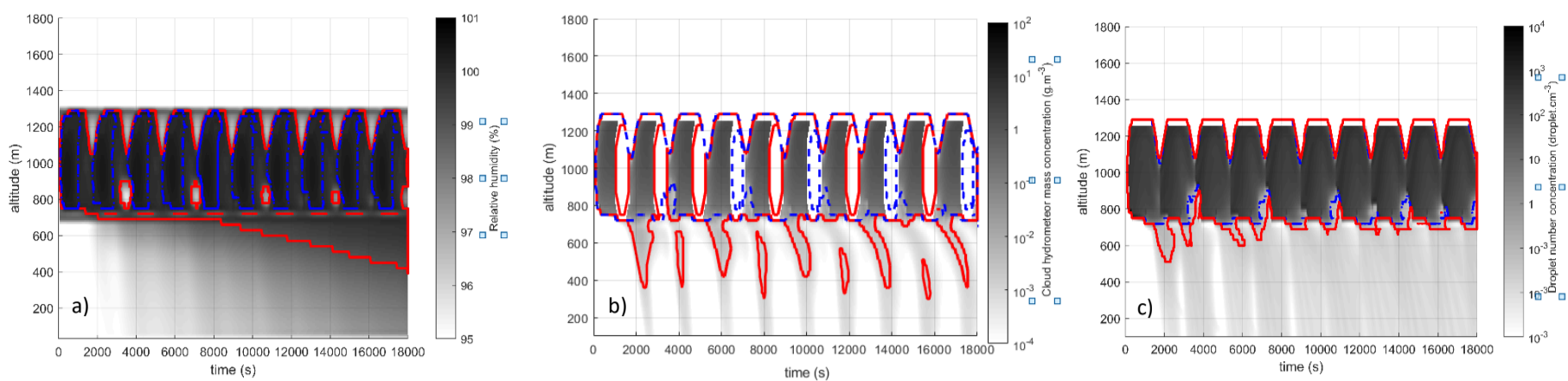
Figure 13. Test of different criteria to establish the contours of the simulated stratus.
a) threshold based on relative humidity: (---) $RH > 99\%$; (—)$RH > 100\%$.
b) threshold based on the mass concentration of hydrometeors with a diameter less than 64 μm: (- - -) mass concentration of cloud hydrometeors $> 0.01\ g.m^{-3}$; (—) mass concentration of cloud hydrometeors$> 0.001 g.m^{-3}$;
c) threshold based on the concentration of hydrometeors: (- - -); $\int d\mathbb{N} > 0.1\ cm^{-3}$; (—) $\int d\mathbb{N} + d\mathfrak{N} > 0.03\ cm^{-3}$.

Based on these results, it is more difficult to delineate the contours of this stratus than for the cumulonimbus. This is because, for these three criteria, only the droplets concentration shows a clear demarcation between precipitation and cloud zone. Moreover, only this criterion gives stable cloud contours, regardless of the threshold value selected. This difference with respect to the cumulonimbus is mainly due to the size of the precipitating hydrometeors, which are much larger in the case of cumulonimbus. Figure 14 shows that the particle size distribution mode in number of raindrops, for the cumulonimbus, is close to a diameter of 1 mm, whereas it is 100 μm for the stratus. It is therefore easier with a cumulonimbus than with a stratus to define a size threshold distinguishing droplet (belonging to the cloud) from raindrops (belonging to precipitation). The criterion based on the mass concentration of hydrometeors exceeding 64 μm is therefore less effective under a stratus than under a cumulonimbus. To explain the poor performance of the criterion based on relative humidity, again it is the particle size that counts. As the droplets under the stratus are smaller than under the cumulonimbus, their velocities are lower, and they reside longer in the atmosphere – about 10 times longer. This longer residence time promotes the increase in relative humidity under the cloud, and humidity saturation under the cloud. This makes it difficult to use this criterion to determine the boundary between rain and cloud for a stratus.
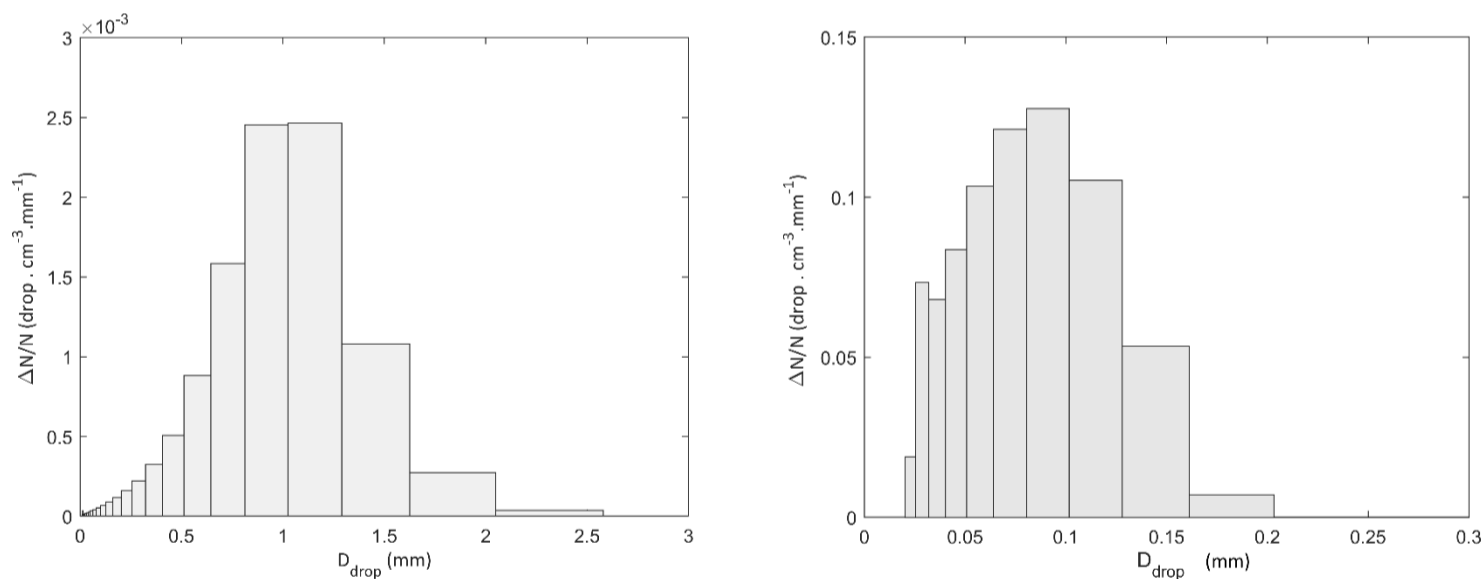
Figure 14. Particle size distributions of raindrops determined by the DESCAM model at ground level
Left: For cumulonimbus at time t=3000 s
Right: For cumulonimbus at time t=8200 s

As previously, for the cumulonimbus, we search for a criterion to delimit cloud from rain. The same parameters as in section 2.1 are investigated and presented in Figure 15, 16 and 17.

388
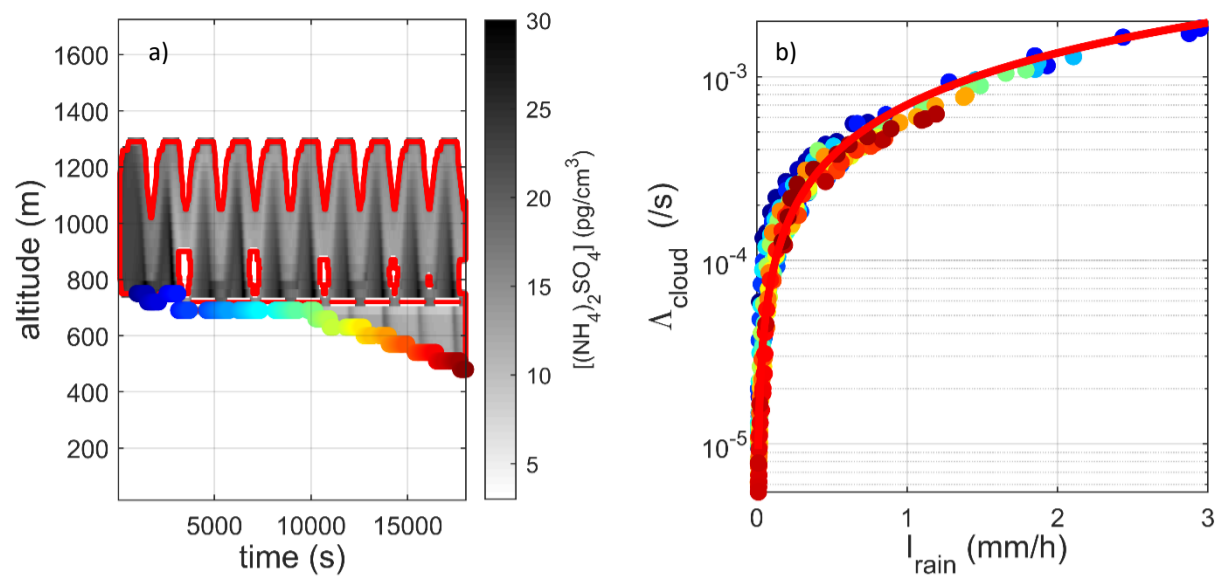
Figure 15. On the left: spatial-temporal distribution of the ammonium sulfate concentration in the cloud contour (—cloud contour for a relative humidity above 99%). On the right: correlation between the scavenging coefficient and the precipitation intensity determined at the base of the cloud, (—) adjusted by a power law.

392
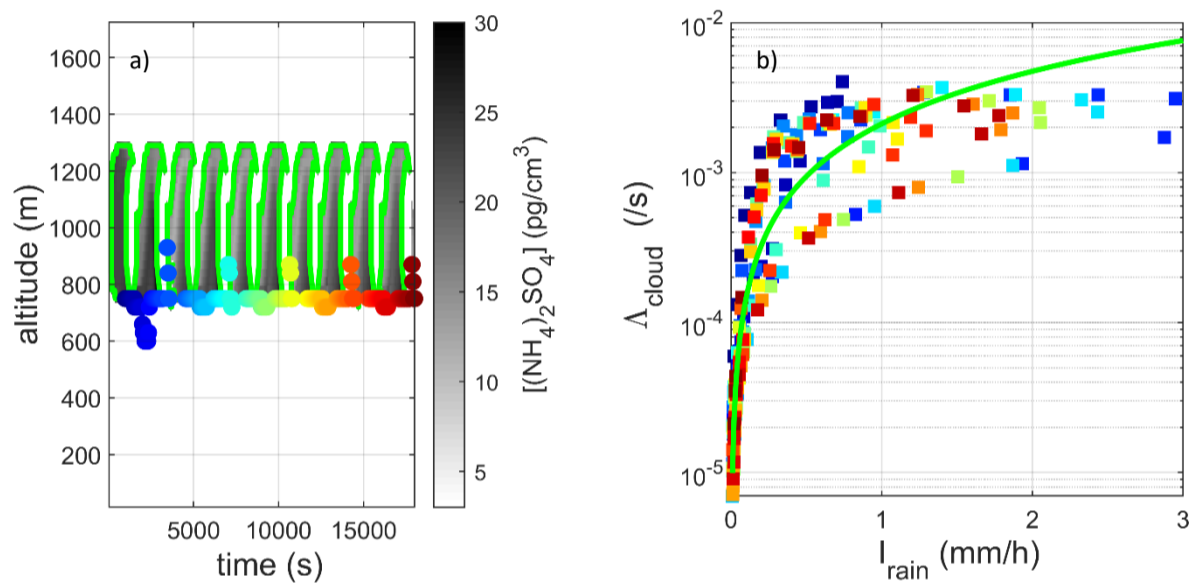
Figure 16. On the left: spatial-temporal distribution of the ammonium sulfate concentration in the cloud contour (—) criterion based on the mass concentration of hydrometeors with a diameter greater than 64 μm with a threshold set at 0.01 g.m $^{-3}$). On the right: correlation between the scavenging coefficient and the precipitation intensity determined at the base of the cloud, (—) adjusted by a power law.

396
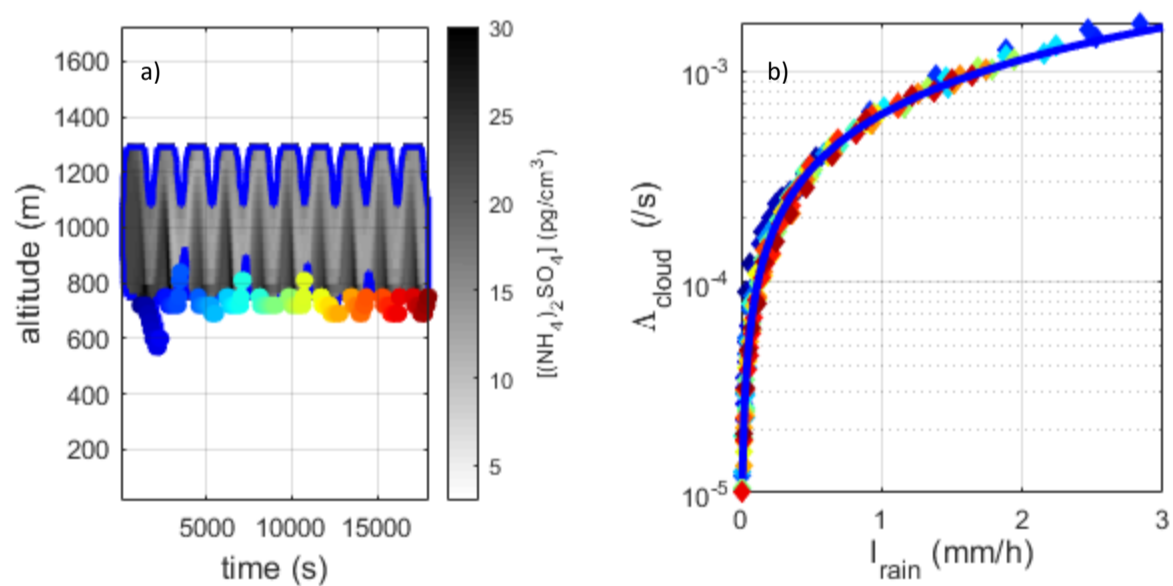
Figure 17. On the left: spatial-temporal distribution of the ammonium sulfate concentration in the contour of the cloud (criterion based on the concentration of hydrometeors with a threshold set at 0.01 particle.cm^3). On the right: correlation between the scavenging coefficient and the precipitation intensity determined at the base of the cloud, (—) adjusted by a power law.

400

401 In these three figures, we observe that the contour introduced by Hiron (2017) for cumulonimbus (based on a separation between cloud water and
402 precipitation water, on the basis of a criterion on the size of hydrometeors, cf. section 1.2) is no longer applicable for the stratus, and gives highly dispersed
403 scavenging coefficient results, particularly for low rain intensity ($I < 2\ mm.h^{-1}$). This is because, for this stratus, it is difficult to establish a strict boundary

between a raindrop and a cloud droplet, based on their size. However, the other two criteria yield bijective and similar relationships, both in terms of the cloud contours (Figure 15.a and Figure 17.a) and the adjusted power laws (Table 2). Unlike cumulonimbus, stratus contours appear to be reliable using a criterion based on relative humidity. This difference is related to the intensities of vertical flows in the cumulonimbus. Indeed, we observe in Figure 5 that, in the simulated cumulonimbus, the downdraft flows can be very intense (up to 5 m.s^{-1}), transporting to the base of the cloud air masses with a lower mixing ratio and hence lower relative humidity.

Table 2. Adjustment of scavenging coefficients by power laws for the three types of contours studied.

Contour type	Power law adjustments
Based on relative humidity **(Figure 15)**	$\Lambda_{cloud}^{m} = 7.03 \times 10^{-4} I^{0.94}$
Based on mass concentration of **cloud hydrometeors** **(Figure 16)**	$\Lambda_{cloud}^{m} = 2.10 \times 10^{-3} I^{1.16}$
Based on hydrometeor **concentration** **(Figure 17)**	$\Lambda_{cloud}^{m} = 6.24 \times 10^{-4} I^{0.86}$

These calculations show that, regardless of the type of simulated cloud, cumulonimbus or stratus, the criterion based on the hydrometeor concentration makes it possible to yield cloud contours that are both stable (with little variation when the threshold value is varied), and for which the relationship between the scavenging coefficient and the rainfall intensity is the most biunivocal (Figure 8, Figure 9 and Figure 10 for cumulonimbus and Figure 15, Figure 16 and Figure 17 for stratus). This criterion is not directly accessible in meteorological models; however, examination of Figure 10 and Figure 17 suggests that the cloud base remains stable over time. It would therefore be possible to assess the altitude at which critical supersaturation is reached, and to consider this altitude constant over a period that depends on the ratio between the size of the grid cell and the velocity of the horizontal flows.

2.3. Comparison with the literature and unification of the scavenging coefficient scheme for a cumulonimbus and a stratus

There is insufficient data to compare our theoretical findings with field study data. Few experimental data have established *in situ* scavenging coefficients for different types of clouds. Based on caesium-137 deposition measured following the Fukushima Daiichi accident, Leadbetter *et al.*, (2015) used the Met Office dispersion model: NAME (Numerical Atmospheric-dispersion Modelling Environment) for the dispersion of the radioactive plume emitted during the accident, considering the meteorological data from the ECMWF model. The authors managed to determine the cloud scavenging coefficient which best suits the ground measurements of deposition (Kinoshita *et al.,* 2011). In the same general approach, but using the IRSN LdX dispersion model (Quélo *et al.*, 2007 and Groëll *et al.*, 2014) and meteorological data from MRI (Sekiyama *et al.*, 2017), Quérel *et al*. (2021) established a very similar scavenging coefficient. These two schemes are compared in Figure 18. The comparison is made using the κ value of ammonium sulfate. This decision is based on the findings of the Kaneyasu et al. (2012) study, which demonstrated the long-distance transport of cesium-137 by these particles - a distance particularly relevant for in-cloud scavenging.
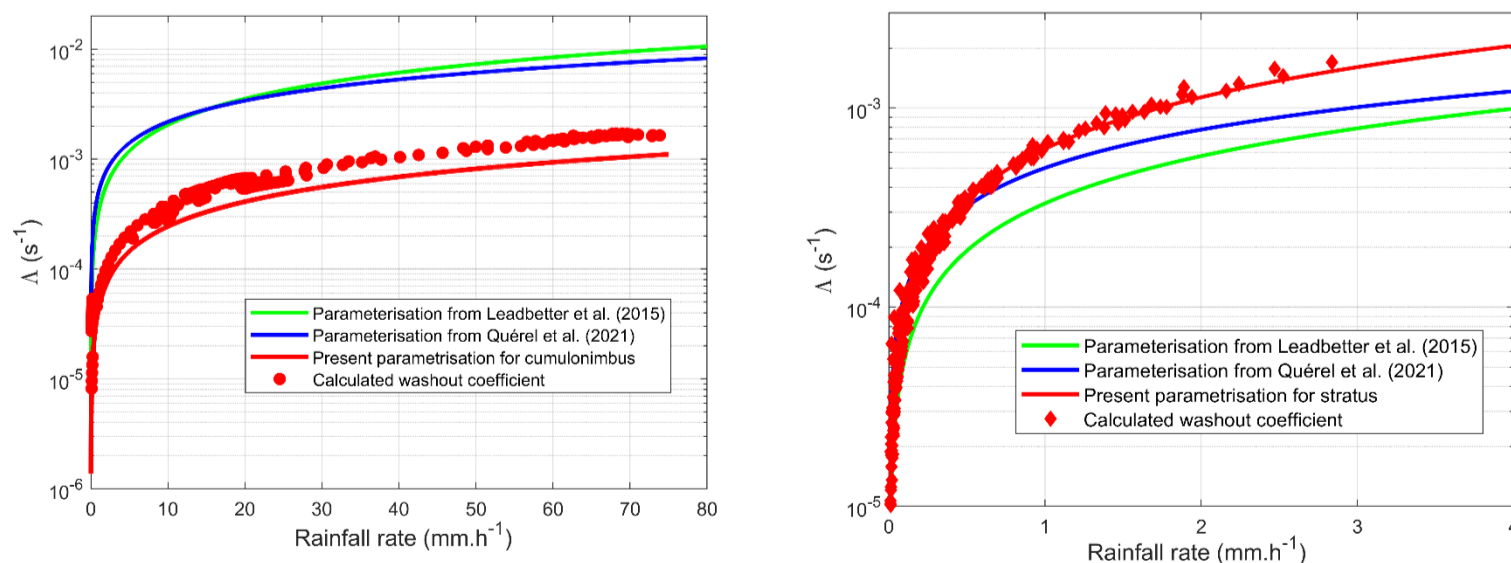
Figure 18. Comparison of the parameterisations established respectively for a cumulonimbus (left) and a stratus (right) with the parameterisations established by Leadbetter *et al.*, 2015 and Quérel *et al*., 2021 following the Fukushima accident.

433 In this figure, we observe that the application of our scheme to a stratus (Figure 18, on the right), concords excellently with the parametrisation of scavenging

434 by clouds established following the Fukushima accident; in particular the parametrisation of Quérel *et al*., (2021). However, the application of our approach

435 to cumulonimbus presents much greater differences. Indeed, over the entire rainfall intensity range, our results are on average six times lower than the

436 correlations of Leadbetter *et al.,* (2015) and Quérel *et al.,* (2021). Two questions therefore arise:

437 First, was there scavenging by cumulonimbus during the Fukushima accident? This would explain why it is difficult to compare our parametrisation of

438 scavenging by cumulonimbus with those deduced during the Fukushima accident.

439 Next, why, for the same rainfall intensity, do our calculations show that cumulonimbus scavenges less than stratus?

440 We will therefore address these two questions.

441 **Was there scavenging by cumulonimbus during the Fukushima accident?**

442 To answer this question, let us consider the distribution of rainfall intensities diagnosed from radar measurements by Saito *et al.*, (2015) during March 2011

443 in the Fukushima region (Figure 19). These results show that 80% of rain episodes diagnosed corresponded to rainfall intensities of less than 1.5 mm.h^{-1},

444 and 97% to intensities of less than 3.5 mm.h^{-1} (range of rainfall intensity produced at the base of the simulated stratus, Figure 15) and less than 0.01% had

445 intensities of more than 10 mm.h^{-1}. In view of these results, it is not possible to completely exclude the presence of rain issuing from cumulonimbus over

446 the period of the accident; however, if there was any, its contribution to the construction of the parameterisation of Leadbetter *et al*. (2015) and Quérel *et*

447 *al*. (2021) is negligible.
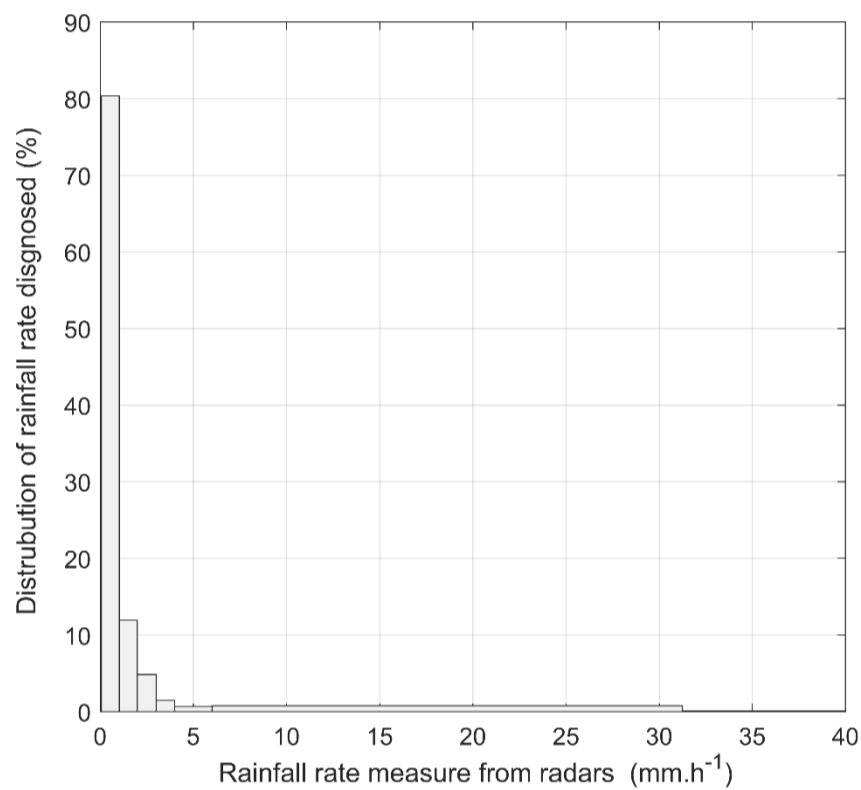
448

449 Figure 19. Distribution of rainfall intensity measured in the Fukushima region during March 2011 (Sekiyama *et al*., 2017).

450

451 **How to unify the scavenging coefficient scheme for a cumulonimbus and a stratus?**

452 Our calculations show that cumulonimbus scavenges less than stratus under the same rainfall intensity. How can we understand this and unify the two

453 equations? This phenomenon can be attributed to the significantly higher level of supersaturation observed in cumulonimbus clouds (Figure 7.a) compared

454 to that in stratus cloud (Figure 13.a). Hence, if the supersaturation is higher, as is the case for cumulonimbus, for the same activated aerosol mass, these

455 particles are diluted in a larger mass of water, as the condensation is also much greater (in reality, the activated aerosol mass increases significantly since,

456 as we have indicated previously, the activation diameter of the aerosols decreases as supersaturation increases). Let us therefore examine the impact of

457 this effect of vapour condensation on the deduced parameterisation. In the DESCAM model, condensation is modelled by Equation 18. This equation is taken

458 from Pruppacher *et al*. (1998, chapter 13, section 2). It results from the vapour diffusion equation on a droplet of diameter $\mathcal{D}_{drop}$ in the air with

459 supersaturation $\mathcal{S}$ and temperature T_{∞}, considering the thermodynamic equilibrium of the suspended drop within air using the κ-Köhler theory.

$$\begin{cases} \dfrac{d\mathcal{D}_{drop}}{dt} = \dfrac{4}{\mathcal{D}_{drop}} \dfrac{\mathcal{S} - y}{\dfrac{\rho_w \mathcal{R} T_\infty}{p_{sat,w} \mathfrak{D}_v M_w} + \dfrac{\mathcal{O}n\rho_w}{kT_\infty}\left(\dfrac{\mathcal{O}n\rho_w}{\mathcal{R}T_\infty} - 1\right)} \\[3em] y = \dfrac{4\,\sigma_{w,\mathcal{D}_{drop}} M_w}{\rho_w \mathcal{R} T_\infty \mathcal{D}_{drop}} - \kappa \dfrac{d_{ap}^{dry\,3}}{\mathcal{D}_{drop}^{\,3}} \end{cases} \qquad \text{Equation 18}$$

460

In this equation $\mathcal{R}$ is the ideal gas constant, $p_{sat,w}$ the saturating vapour pressure, d_{ap}^{dry} the dry diameter of the aerosol, $\mathcal{O}n$ the latent heat of vaporisation of the water, $\sigma_{w,\mathcal{D}_{drop}}$ the surface tension, k the thermal conductivity of the air, M_w and ρ_w the molar mass and density of the water vapour, and finally $\mathfrak{D}_v$ the diffusion coefficient of the vapour in water in the air. As the Kelvin effect (linked to the curvature of the interface) and the solute effect become very quickly negligible after activation of the aerosol, this equation can be greatly simplified and reduced to: $\mathcal{D}_{drop} d\mathcal{D}_{drop} = \mathbb{C}.\mathcal{S} dt$, where $\mathbb{C}$ is a constant, enabling it to be integrated analytically, Δt the lifetime of the drop, to give: $\mathcal{D}_{drop} = \sqrt{\mathcal{D}_{drop,t_0}^2 + 2\mathbb{C}.\mathcal{S} \cdot \Delta t}$. Thus, to assess the effect of dilution of the aerosol in the droplet due to condensation, we can write:

$$\frac{\mathcal{D}_{drop}^{stratus\,2}}{\mathcal{D}_{drop}^{cumulonimbus\,2}} = \frac{\mathcal{D}_{drop,t_0}^2 + 2\mathbb{C}.\langle \mathcal{S} \rangle_{stratus} \cdot \Delta t_{stratus}}{\mathcal{D}_{drop,t_0}^2 + 2\mathbb{C}.\langle \mathcal{S} \rangle_{cumulonimbus} \cdot \Delta t_{cumulonimbus}} \qquad \text{Equation 19}$$

$\Delta t_{stratus}$ and $\Delta t_{cumulonimbus}$ are respectively the lifetime of the drop into a stratus and a cumulonimbus. Attention, in this equation, $\mathcal{D}_{drop}^{stratus}$ and $\mathcal{D}_{drop}^{cumulonimbus}$ are not the diameters of the droplets in the stratus and in the cumulonimbus, but the diameters they would have had, if only the condensation mechanism had caused them to grow. We are in fact seeking to assess how large will be the dilution of aerosol material in the droplets related to vapour condensation. There are other mechanisms modelled in DESCAM (such as coalescence or riming, Figure 2) that lead to the growth of hydrometeors, without necessarily diluting the aerosols in the droplets. If there had only been the condensation mechanism, we could have used Figure 14 directly to assess this dilution. When precipitation begins, further simplification can still be made because $\mathcal{D}_{drop,t_0}^2 \ll \mathcal{D}_{drop}^{stratus\,2} < \mathcal{D}_{drop}^{cumulonimbus\,2}$. Finally, we can write:

$$\frac{\mathcal{D}_{drop}^{stratus\,2}}{\mathcal{D}_{drop}^{cumulonimbus\,2}} = \frac{\langle \mathcal{S} \rangle_{stratus} \cdot \Delta t_{stratus}}{\langle \mathcal{S} \rangle_{cumulonimbus} \cdot \Delta t_{cumulonimbus}} \qquad \text{Equation 20}$$

In this equation, the lifetimes $\Delta t_{stratus}$ and $\Delta t_{cumulonimbus}$ are therefore the durations necessary for the formation of precipitation under the cloud. These durations are assimilated to the duration of precipitation formation. For each of the types of cloud, we observe in Figure 6.a and Figure 12.a that these durations are very similar (≈ 2200 s), which allows us to write:

$$\frac{\mathcal{D}_{drop}^{stratus}}{\mathcal{D}_{drop}^{cumulonimbus}} = \sqrt{\frac{\langle \mathcal{S} \rangle_{stratus}}{\langle \mathcal{S} \rangle_{cumulonimbus}}} \qquad \text{Equation 21}$$

The numerical application of this equation highlights a condensation growth ratio of a factor 2.3 between cumulonimbus and stratus. In mass, this coefficient corresponds to a dilution factor of 12. However, Figure 18 shows that, with this new approach, we can calculate that cumulonimbus scavenges 6 times less than stratus. This explanation is therefore satisfactory in view of all the hypotheses that have been made, especially since we have considered that the activated aerosol mass remained constant when supersaturation increased. We therefore propose a new generic parametrisation to any type of cloud, which this time considers this condensation-related dilution effect, Equation 22. This scavenging scheme is therefore corrected by a coefficient $1/\langle \mathcal{S} \rangle_{cloud}^{3/2}$ which characterises the dilution related to the growth of droplets by condensation:

$$\Lambda_{cloud}^m = \frac{5 \times 10^{-8}}{\langle \mathcal{S} \rangle_{cloud}^{3/2}} I^{0.75} \qquad \text{Equation 22}$$

The application of this new correlation, presented in Figure 20 shows an excellent match both for the cumulonimbus and for the simulated stratus. It remains to be considered whether supersaturation is accessible in the NWPs and, if so, if the horizontal resolutions of 1 to 10 km of such models are sufficiently representative of a real cloud.
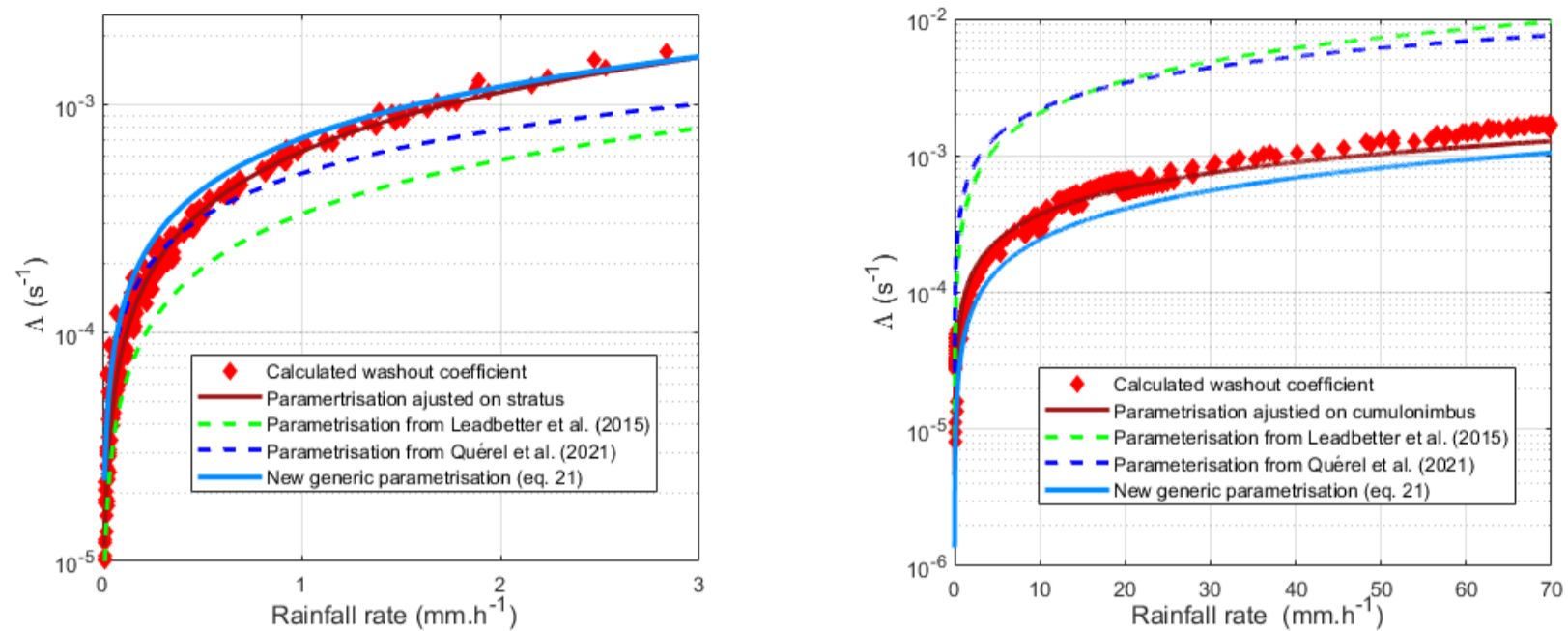
Figure 20. Comparison of the newly developed correlation Equation 22 with the scavenging modelled by DESCAM for a cumulonimbus and a stratus.

3. Conclusions

The in-cloud scavenging scheme established in this article shows a dependence on rain intensity and average supersaturation in the cloud. Supersaturation allows the scheme to be applicable to both cumulonimbus and stratus clouds. If supersaturation in the cloud is not accessible, it is still possible to apply a different scheme for convective clouds and stratiform clouds. But, since this boundary between the two types of cloud may be ambiguous, it will be preferable to apply the scheme with supersaturation if available.

This scavenging scheme is based on the DESCAM microphysical cloud model. This model allows fine-scale description of the life cycle of a cloud up to precipitation development. It tracks particles, crystals, and droplets particle size distributions and models all the water phase changes and, above all, how aerosol particles impact them. The in-cloud scavenging scheme is established by calculating the mass fluxes of particle material exiting the cloud being included in precipitation hydrometeors (both liquid and solid) and based on the mass of particles initially present in the cloud volume.

This calculation of cloud volume has proved to be a complex issue, in particular for establishing the altitude of the cloud base, especially when rain occurs. The most relevant method to identify cloud base in this study has been proven to be the one using the number of hydrometeors, rather than the relative humidity or the mass of the hydrometeors. The problem with this method is that this information on the number is not available for most of the NWPs. The use of the in-cloud scavenging scheme must be based on a diagnostic independent of the altitude of the base – and the summit – of the cloud.

In the case of stratus cloud, the parametrisation obtained with DESCAM is close to those currently used in the NAME and LdX atmospheric dispersion models, which were established on the basis of the Fukushima accident. As the precipitation that caused deposition of radioactive particles following the accident was largely generated by stratiform clouds, this study confirms *a posteriori* the choice of the in-cloud deposition scheme used to study radioactive deposition following the Fukushima accident and can be extended to all types of cloud.

In future works, this deposition scheme will be used with confidence to study deposition. As an example, it can be used for the deposition of radon progeny (Quérel *et al.,* 2022), in order to statistically measure the impact of this scheme in relation to the existing corpus.

Beyond the applications and validations of the scheme described in this article, the scheme itself is currently being refined. First of all, we are working on establishing an in-cloud scavenging rate that will depend on particle size. This important issue was discussed in section 1.3, and requires some modifications to the model to establish a model spectrally. This will make it possible to apply a finer-scale scheme to the atmospheric models with a spectral representation of the particles.

The influence of the coefficient κ of the κ-Köhler theory can be also examined. This will make it possible to measure the importance of the physical-chemical properties of the particles: what error is made by applying the same scavenging rate for a hygroscopic aerosol (salt or sulfate) and a non-hygroscopic aerosol (soot, desert dust).

The initial particle size distribution of aerosols could also have a significant influence on the final scavenging rate. A distribution centred on 100 nm will not create the same cloud as the same total mass centred around 5 μm particles. This aspect must be assessed.

521   The question of evaporation of droplets between the cloud base and the ground has not yet been addressed. The scheme developed is based on the

522   precipitation intensity at the cloud base, but in the models the precipitation intensity is diagnosed on the ground. This is important for the applicability of

523   the scheme and this difference can lead to errors, especially in the event of high droplet evaporation.

524   Finally, it is not yet established that this scheme is as effective when applied to a model whose spatial resolution is lower than that of DESCAM, as is the

525   case for all Climate (GCM) and Transport (ATM) models.

526   The work still to be carried out will make it possible to best define the scope of validity of this new scheme for in-cloud aerosol scavenging, as well as the

527   uncertainties associated with this model. This will enable the scheme to be used in full knowledge of the facts and according to the highest scientific

528   standards.

529

530

Competing interests

531

532   The contact author has declared that none of the authors has any competing interests.

533

References

Adachi K, Kajino M, Zaizen Y, Igarashi Y. Emission of spherical cesium-bearing particles from an early stage of the Fukushima nuclear accident. Sci Rep. 2013;3:2554. doi: 10.1038/srep02554. PMID: 23989894; PMCID: PMC3757362.

Asai, T., & Kasahara, A. (1967). A theoretical study of the compensating downward motions associated with cumulus clouds. *Journal of Atmospheric Sciences*, *24*(5), 487-496.

American Meterological Society, 2020b: Glossary of meteorology: cloud. Website, accessed on October 21, 2020, URL http://glossary.ametsoc.org/wiki/cloud.

Baklanov, A., & Sørensen, J. H. (2001). Parameterisation of radionuclide deposition in atmospheric long-range transport modelling. Physics and Chemistry of the Earth, Part B: Hydrology, Oceans and Atmosphere, 26(10), 787-799.

Bigg, E. K. (1953). The formation of atmospheric ice crystals by the freezing of droplets. *Quarterly Journal of the Royal Meteorological Society*, *79*(342), 510-519.

Beard, K. V. (1974). Experimental and numerical collision efficiencies for submicron particles scavenged by small raindrops. *Journal of Atmospheric Sciences*, *31*(6), 1595-1603.

Bergeron, T. (1928). *Über die dreidimensional verknüpfende Wetteranalyse. 1. Prinzipielle Einführung in das Problem der Luftmassen-und Frontenbildung*. na. Bony, S., & Dufresne, J. L. (2005). Marine boundary layer clouds at the heart of tropical cloud feedback uncertainties in climate models. *Geophysical Research Letters*, *32*(20).

Clark, M. J., & Smith, F. B. (1988). Wet and dry deposition of Chernobyl releases. *Nature*, *332*(6161), 245-249.

Costa, M. J., Salgado, R., Santos, D., Levizzani, V., Bortoli, D., Silva, A. M., & Pinto, P. (2010). Modelling of orographic precipitation over Iberia: a springtime case study. *Advances in Geosciences*, *25*, 103-110.

Croft, B., Lohmann, U., Martin, R. V., Stier, P., Wurzler, S., Feichter, J., ... & Ferrachat, S. (2010). Influences of in-cloud aerosol scavenging parameterizations on aerosol concentrations and wet deposition in ECHAM5-HAM. *Atmospheric Chemistry and Physics*, *10*(4), 1511-1543.

De Cort, M. (1998). Atlas of caesium deposition on Europe after the Chernobyl accident.

Dépée, A., Lemaitre, P., Gelain, T., Mathieu, A., Monier, M., & Flossmann, A. (2019). Theoretical study of aerosol particle electroscavenging by clouds. *Journal of Aerosol Science*, *135*, 1-20.

Dépée, A. (2019). *Etude expérimentale et théorique des mécanismes microphysiques mis en jeu dans la capture des aérosols radioactifs par les nuages* (Doctoral dissertation, Université Clermont Auvergne [2017-2020]).

Dépée, A., Lemaitre, P., Gelain, T., Monier, M., & Flossmann, A. (2021). Laboratory study of the collection efficiency of submicron aerosol particles by cloud droplets–Part I: Influence of relative humidity. *Atmospheric Chemistry and Physics*, *21*(9), 6945-6962.

Dépée, A., Lemaitre, P., Gelain, T., Monier, M., & Flossmann, A. (2021). Laboratory study of the collection efficiency of submicron aerosol particles by cloud droplets–Part II: Influence of electric charges. *Atmospheric Chemistry and Physics*, *21*(9), 6963-6984.

Dye, J. E., Jones, J. J., Winn, W. P., Cerni, T. A., Gardiner, B., Lamb, D., ... & Saunders, C. P. R. (1986). Early electrification and precipitation development in a small, isolated Montana cumulonimbus. *Journal of Geophysical Research: Atmospheres*, *91*(D1), 1231-1247.

Ervens, B. (2015). Modeling the processing of aerosol and trace gases in clouds and fogs. *Chemical reviews*, *115*(10), 4157-4198.

Findeisen, Z. (1938). Kolloid meteorologische vorgange bei neiderschlags-bildung. *Meteorologische Zeitschrift*, *55*, 121.

Flossmann, A. I., Hall, W. D., & Pruppacher, H. R. (1985). A theoretical study of the wet removal of atmospheric pollutants. Part I: The redistribution of aerosol particles captured through nucleation and impaction scavenging by growing cloud drops. *Journal of Atmospheric Sciences*, *42*(6), 583-606.

Flossmann, A. I., Pruppacher, H. R., & Topalian, J. H. (1987). A theoretical study of the wet removal of atmospheric pollutants. Part II: The uptake and redistribution of (NH 4) 2 SO 4 particles and SO 2 gas simultaneously scavenged by growing cloud drops. *Journal of Atmospheric Sciences*, *44*(20), 2912-2923.

Flossmann, A. I., & Pruppacher, H. R. (1988). A theoretical study of the wet removal of atmospheric pollutants. Part III: The uptake, redistribution, and deposition of (NH 4) 2 SO 4 particles by a convective cloud using a two-dimensional cloud dynamics model. *Journal of Atmospheric Sciences*, *45*(13), 1857-1871.

Flossmann, A. I. (1998). Clouds and pollution. *Pure and applied chemistry*, *70*(7), 1345-1352.

576 Flossmann, A. I., & Wobrock, W. (2010). A review of our understanding of the aerosol–cloud interaction from the perspective of a bin resolved cloud scale

577 modelling. *Atmospheric Research*, *97*(4), 478-497.

578 Groëll, J., Quélo, D., & Mathieu, A. (2014). Sensitivity analysis of the modelled deposition of 137 Cs on the Japanese land following the Fukushima

579 accident. International Journal of Environment and Pollution, 55(1-4), 67-75.

580 Hertel, O., Christensen, J., Runge, E. H., Asman, W. A., Berkowicz, R., Hovmand, M. F., & Hov, Ø. (1995). Development and testing of a new variable scale air

581 pollution model—ACDEP. *Atmospheric Environment*, *29*(11), 1267-1290.

582 Hirsch, E., Koren, I., Levin, Z., Altaratz, O., & Agassi, E. (2014). On transition-zone water clouds. *Atmospheric Chemistry and Physics*, *14*(17), 9001-9012.

583 Hiron, T., & Flossmann, A. I. (2015). A study of the role of the parameterization of heterogeneous ice nucleation for the modeling of microphysics and

584 precipitation of a convective cloud. *Journal of the Atmospheric Sciences*, *72*(9), 3322-3339.

585 Hiron, T. (2017). *Experimental and modeling study of heterogeneous ice nucleation on mineral aerosol particles and its impact on a convective cloud* (Doctoral

586 dissertation, Université Clermont Auvergne).

587 Kaneyasu, N., Ohashi, H., Suzuki, F., Okuda, T., & Ikemori, F. (2012). Sulfate aerosol as a potential transport medium of radiocesium from the Fukushima

588 nuclear accident. *Environmental science & technology*, *46*(11), 5720-5726.

589 Kerker, M., & Hampl, V. (1974). Scavenging of Aerosol Particles by a Failing Water Drop and Calculation of Washout Coefficients. *Journal of Atmospheric*

590 *Sciences*, *31*(5), 1368-1376.

591 Kinoshita, N., Sueki, K., Sasa, K., Kitagawa, J. I., Ikarashi, S., Nishimura, T., ... & Yamagata, T. (2011). Assessment of individual radionuclide distributions from

592 the Fukushima nuclear accident covering central-east Japan. *Proceedings of the National Academy of Sciences*, *108*(49), 19526-19529.

593 Knight, C. A. (1982). The cooperative convective precipitation experiment (CCOPE), 18 May–7 August 1981. *Bulletin of the American Meteorological*

594 *Society*, *63*(4), 386-398.

595 Koop, T., Luo, B., Tsias, A., & Peter, T. (2000). Water activity as the determinant for homogeneous ice nucleation in aqueous solutions. *Nature*, *406*(6796),

596 611-614.

597 Laguionie, P., Roupsard, P., Maro, D., Solier, L., Rozet, M., Hébert, D., & Connan, O. (2014). Simultaneous quantification of the contributions of dry, washout

598 and rainout deposition to the total deposition of particle-bound 7Be and 210Pb on an urban catchment area on a monthly scale. Journal of aerosol

599 science, 77, 67-84.

600 Lai, K. Y., Dayan, N., & Kerker, M. (1978). Scavenging of aerosol particles by a falling water drop. *Journal of Atmospheric Sciences*, *35*(4), 674-682.

601 Leadbetter, S. J., Hort, M. C., Jones, A. R., Webster, H. N., & Draxler, R. R. (2015). Sensitivity of the modelled deposition of Caesium-137 from the Fukushima

602 Dai-ichi nuclear power plant to the wet deposition parameterisation in NAME. *Journal of environmental radioactivity*, *139*, 200-211.

603 Leaitch, W., Strapp, J. W., Isaac, G. A., & Hudson, J. G. (1986). Cloud droplet nucleation and cloud scavenging of aerosol sulphate in polluted

604 atmospheres. *Tellus B: Chemical and Physical Meteorology*, *38*(5), 328-344.

605 Lemaitre, P., Quérel, A., Monier, M., Menard, T., Porcheron, E., & Flossmann, A. I. (2017). Experimental evidence of the rear capture of aerosol particles by

606 raindrops. *Atmospheric Chemistry and Physics*, *17*(6), 4159-4176.

607 Leroy, D., Monier, M., Wobrock, W., & Flossmann, A. I. (2006). A numerical study of the effects of the aerosol particle spectrum on the development of the

608 ice phase and precipitation formation. *Atmospheric Research*, *80*(1), 15-45.

609 Leroy, D., Wobrock, W., & Flossmann, A. I. (2007). On the influence of the treatment of aerosol particles in different bin microphysical models: a comparison

610 between two different schemes. *Atmospheric research*, *85*(3-4), 269-287.

611 Meyers, M. P., DeMott, P. J., & Cotton, W. R. (1992). New primary ice-nucleation parameterizations in an explicit cloud model. *Journal of Applied Meteorology*

612 *and Climatology*, *31*(7), 708-721.

613 Monier, M., Wobrock, W., Gayet, J.-F., Flossmann, A., (2006). Development of a detailed microphysics cirrus model for interpretation of the recent INCA

614 campaign. J. Amtos. Sci. 163.

615 Mathieu, A., Korsakissok, I., Quélo, D., Groëll, J., Tombette, M., Didier, D., ... & Isnard, O. (2012). Atmospheric dispersion and deposition of radionuclides

616 from the Fukushima Daiichi nuclear power plant accident. Elements, 8(3), 195-200.

617 MRI, 2015. JMA-RATM Technical Report, vol. 76.

618 Palmer, T. (2014). Climate forecasting: Build high-resolution global climate models. *Nature*, *515*(7527), 338-339.

619   Petters, M. D., & Kreidenweis, S. M. (2007). A single parameter representation of hygroscopic growth and cloud condensation nucleus activity. *Atmospheric*
620   *Chemistry and Physics*, *7*(8), 1961-1971.

621   Petroff, A., Mailliat, A., Amielh, M., & Anselmet, F. (2008). Aerosol dry deposition on vegetative canopies. Part I: review of present knowledge. *Atmospheric*
622   *Environment*, *42*(16), 3625-3653.

623   Pranesha, T. S., & Kamra, A. K. (1996). Scavenging of aerosol particles by large water drops: 1. Neutral case. *Journal of Geophysical Research:*
624   *Atmospheres*, *101*(D18), 23373-23380.

625   Pruppacher, H. R., Klett, J. D., & Wang, P. K. (1998). Microphysics of clouds and precipitation. 2nd ed., Atmospheric and Oceanographic Sciences Library,
626   Kluwer Academic Publishers, doi:10.1080/02786829808965531.

627   Quélo, D., Krysta, M., Bocquet, M., Isnard, O., Minier, Y., & Sportisse, B. (2007). Validation of the Polyphemus platform on the ETEX, Chernobyl and Algeciras
628   cases. *Atmospheric environment*, *41*(26), 5300-5315.

629   Quérel, A., Monier, M., Flossmann, A. I., Lemaitre, P., & Porcheron, E. (2014). The importance of new collection efficiency values including the effect of rear
630   capture for the below-cloud scavenging of aerosol particles. *Atmospheric research*, *142*, 57-66.

631   Quérel, A., Quelo, D., Roustan, Y., & Mathieu, A. (2021). Sensitivity study to select the wet deposition scheme in an operational atmospheric transport
632   model. *Journal of Environmental Radioactivity*, *237*, 106712.

633   Quérel, A., Meddouni, K., Quélo, D., Doursout, T., Chuzel, S., 2022. Statistical approach to assess radon-222 long-range atmospheric transport modelling and
634   its associated gamma dose rate peaks, in: Advances in Geosciences. Presented at the Geoscience applications of environmental radioactivity - EGU General
635   Assembly 2021, Online, 19–30 April 2021, Copernicus GmbH, pp. 109–124.

636   Saito, K., Shimbori, T., & Draxler, R. (2015). JMA's regional atmospheric transport model calculations for the WMO technical task team on meteorological
637   analyses for Fukushima Daiichi Nuclear Power Plant accident. *Journal of environmental radioactivity*, *139*, 185-199.

638   Sassen, K., and B. S. Cho, 1992: Subvisual-thin cirrus lidar dataset for satellite verification and climatological research. J. Appl. Meteorol., 31, 1275–1285,
639   doi:10.1175/1520-0450(1992) 031<1275:STCLDF>2.0.CO;2, https://doi.org/10.1175/1520-0450(1992)031<1275:STCLDF>
640   2.0.CO;2.

641   Saito, K., Shimbori, T., & Draxler, R. (2015). JMA's regional atmospheric transport model calculations for the WMO technical task team on meteorological
642   analyses for Fukushima Daiichi Nuclear Power Plant accident. Journal of environmental radioactivity, 139, 185-199.

643   Sievering, H., Van Valin, C. C., Barrett, E. W., & Pueschel, R. F. (1984). Cloud scavenging of aerosol sulfur: Two case studies. *Atmospheric Environment*
644   *(1967)*, *18*(12), 2685-2690.

645   Slinn, W. G. N.: Some approximations for the wet and dry removal of particles and gases from the atmosphere, Water Air Soil Poll.,7, 513–543, 1977.

646   Spänkuch, D., Hellmuth, O., & Görsdorf, U. (2022). What is a cloud? Toward a more precise definition?. *Bulletin of the American Meteorological Society*.

647   Stephan, K., Klink, S., & Schraff, C. (2008). Assimilation of radar-derived rain rates into the convective-scale model COSMO-DE at DWD. *Quarterly Journal of*
648   *the Royal Meteorological Society: A journal of the atmospheric sciences, applied meteorology and physical oceanography*, *134*(634), 1315-1326.

649   Textor, C., Schulz, M., Guibert, S., Kinne, S., Balkanski, Y., Bauer, S., ... & Tie, X. (2006). Analysis and quantification of the diversities of aerosol life cycles
650   within AeroCom. *Atmospheric Chemistry and Physics*, *6*(7), 1777-1813.

651   Wegener, A. (1911). *Thermodynamik der atmosphäre*. JA Barth.

652   Vali, G., DeMott, P. J., Möhler, O., & Whale, T. F. (2015). A proposal for ice nucleation terminology. *Atmospheric Chemistry and Physics*, *15*(18), 10263-10270.

653   Vohl, O., Mitra, S. K., Wurzler, S. C., & Pruppacher, H. R. (1999). A wind tunnel study of the effects of turbulence on the growth of cloud drops by collision
654   and coalescence. *Journal of the atmospheric sciences*, *56*(24), 4088-4099.

655   Wang, H., & Su, W. (2013). Evaluating and understanding top of the atmosphere cloud radiative effects in Intergovernmental Panel on Climate Change (IPCC)
656   Fifth Assessment Report (AR5) Coupled Model Intercomparison Project Phase 5 (CMIP5) models using satellite observations. *Journal of Geophysical*
657   *Research: Atmospheres*, *118*(2), 683-699.

658   WMO. (2014). Guide to Meteorological Instruments and Methods of Observation (CIMO Guide, WMO-No. 8. Wood, R., & Field, P. R. (2011). The distribution
659   of cloud horizontal sizes. Journal of Climate, 24 (18), 4800-4816.

660   Zhang, L., Michelangeli, D. V., & Taylor, P. A. (2004). Numerical studies of aerosol scavenging by low-level, warm stratiform clouds and
661   precipitation. *Atmospheric Environment*, *38*(28), 4653-4665.

662   Zhang, S., Xiang, M., Xu, Z., Wang, L., & Zhang, C. (2020). Evaluation of water cycle health status based on a cloud model. *Journal of cleaner production*, *245*,

663   118850.